Contemporary Mathematics
https://ojs.wiserpub.com/index.php/CM/

Research Article

Jeffrey, Maxwell, and Micropolar Tri-Hybrid Nanofluid Heat and Mass Transfer Behavior of Mixed Convection Flow past a Vertical Porous Surface

Hossam A. Nabwey[1*], Waqar A. Khan[2], Assma S Zaki[3], Amal M. A. EL-Hakiem[3], Ahmed M. Rashad[3], Mohamed M. Awad[1], Abdullah Aldurayhim[1], M. M. Nour[1]

[1] Department of Mathematics, College of Science and Humanities in Al-Kharj, Prince Sattam Bin Abdulaziz University, Al-Kharj, 11942, Saudi Arabia
[2] Department of Pure and Applied Mathematics, Saveetha School of Engineering, Saveetha Nagar, Thandalam, Chennai, Tamilnadu, 602105, India
[3] Department of Mathematics, Faculty of Science, Aswan University, Aswan, 81528, Egypt
E-mail: h.mohamed@psau.edu.sa

Received: 21 October 2025; **Revised:** 24 November 2025; **Accepted:** 2 February 2026

Abstract: This study presents a comparative analysis of heat and mass transfer in mixed convection flow of a tri-hybrid nanofluid past a vertical porous stretching surface. The non-Newtonian base fluid is modeled using three rheological frameworks: Jeffrey, Maxwell, and Micropolar models. Soret and Dufour effects, along with variable temperature and concentration fields, are incorporated. The governing partial differential equations are transformed into nonlinear ordinary differential equations via similarity variables. The resulting system is solved using the MATLAB *bvp4c* finite-difference collocation scheme, ensuring high numerical accuracy and stability. The tri-hybrid nanofluid comprises Multi-Walled Carbon Nanotubes (MWCNTs), Molydenium disulphide (MoS_2), and Graphene Oxide (GO) in water with a total nanoparticle volume fraction of 0.03. Results show that Maxwell fluids provide the highest Nusselt number enhancement (up to 24.6%) under opposing flow, whereas Jeffrey fluids yield superior mass transfer with 18-22% Sherwood number gains in assisting flows. Suction enhances skin friction by 15-20%, while injection reduces boundary-layer thickness by about 30%. A fractional derivative model is also introduced to capture memory and hereditary effects more accurately. The findings offer valuable insights for optimizing thermal systems employing advanced non-Newtonian tri-hybrid nanofluids.

***Keywords*:** heat and mass transport, combined convection, Maxwell, Jeffrey tri-hybrid nanofluid, porous medium, micropolar nanofluid, vertical stretched surface

MSC: 76U05, 76W05, 76D05

1. Introduction

Over the last few decades, many scientists and authors have focused on non-Newtonian fluids due to their applications in industry and engineering. Fluids that don't adhere to Newton's law of motion are identified as non-Newtonian fluids.

Copyright ©2026 Hossam A. Nabwey, et al.
DOI: https://doi.org/10.37256/cm.7220268963
This is an open-access article distributed under a CC BY license
(Creative Commons Attribution 4.0 International License)
https://creativecommons.org/licenses/by/4.0/

Examples include toothpaste, food products, waste fluids, and form oil. The flow and heat transfer properties of these fluids differ significantly from those of Newtonian fluids. The equations governing non-Newtonian fluid flows are notably nonlinear and more complex than the Navier-Stokes equations. This nonlinearity means that closed-form solutions for non-Newtonian fluid flows are typically unattainable in practical scenarios. Jeffrey-Maxwell nanofluids are significant because of their unique stress-relaxation characteristics.

Non-Newtonian fluids exhibit intricate flow dynamics, primarily because additives such as polymers or particles alter their behavior. Unlike Newtonian fluids, whose viscosity a constant, the viscosity of non-Newtonian fluids varies. This variation is influenced by factors such as shear rate, accumulated strain, and the characteristics of the additives, including their concentration, polymer molecular weight, and particle size. Furthermore, flexible polymers tend to stretch during flow, resulting in an elastic response. The advancement of microfluidic devices focuses on miniaturizing assays to examine the biological, physical, and chemical properties of DeoxyriboNucleic Acid (DNA), proteins, and other biopolymers in solution, as well as in cell and bioparticle suspensions. Since analyses are often performed in liquid form, it is essential to account for non-Newtonian flow behavior (see references [1–8]). Choi [9] pioneered the concept of nanofluid by integrating nanoparticles at the nanometer scale into a base fluid. Chen [10] explored the effects of viscous dissipation and heat transfer in a non-Newtonian fluid over a nonlinear stretching surface. Hayat et al. [11] investigated the impact of convective boundary conditions on Magnetohydrodynamic (MHD) nanofluid flow through a porous medium over an exponentially stretching sheet, employing a series solution technique. Alla and Dahab [12] conducted a study of Jeffrey fluid flow over an asymmetric rotating channel using closed-form solutions. They found that shear stress is significantly higher in symmetric channels than in asymmetric ones. Hayat et al. [13] also studied convective heat transfer in two-dimensional boundary-layer flow of an Oldroyd-B fluid over a stretching surface, considering radiation, and found that the temperature profiles of the Oldroyd-B fluid increase with increasing radiation parameter. Irfan and Muhammad [14] discussed a numerical modeling of Bio-convection radiative heat transport flow of MHD Carreau nanofluid. Rashid et al. [15] studied dynamics of solar radiation absorption for Darcy-Forchheimer Carreau nanofluid taking into account variable conductivity with chemical reaction. Hamida et al. [16] explored improved solar thermal energy performance through bioconvection behavior in radiative MHD Maxwell nanofluids including gyrotactic motile microorganisms, while Hamida et al. [17] studied the thermal engineering investigation of MHD Maxwell nanofluid flow drivin by solar radiation with gyrotactic microorganisms and Soret-Dufour effects. Additionally, Double diffusive nanofluid flow in a conduit with a cavity heated from below has been computationally studied by Hussain et al. [18]. Khan et al. [19] analyzed mathematically a three-dimensional forced convective flow over a bidirectionally stretched surface. In a related study, Arif et al. [20] examined heat transfer in engine oil, emphasizing the role of nanoparticles and noting significant advancements in thermal applications. Zeb et al. [21] investigated the activation energy effects under melting conditions, exothermic/endothermic chemical reactions, and tangent hyperbolic nanofluid flow along a moving stretched surface with thermal radiation, while Sulgani and Karimipour [22] studied the enhancement of engine oil properties using nanofluids across varying temperatures. In another investigation, Said et al. [23] explored the key physical characteristics of nanofluid stability, dynamic motion, and heat transfer. Qiu et al. [24] highlighted progress in the thermophysical properties of nanoscale materials, ranging from solid-state materials to colloids. Smith et al. [25] researched the incorporation of aluminum oxide nanoparticles in water filtration systems. Additionally, Asjad et al. [26] introduced a novel approach using fractional derivatives with water-based nanoparticles, focusing on contemporary applications. Aramendiz and Imqam [27] assessed the application of nanofluids containing graphene and silica nanoparticles in drilling processes. Hybrid nanofluids exhibit superior thermal conductivity compared to base liquids and other nanofluids. They have similar applications as traditional nanofluids, as they are created by dispersing two different types of nanoparticles in a base liquid. The term “hybrid nanoparticles” refers to a class of heat transfer fluids developed to enhance heat transfer in various industrial and engineering processes. When comparing hybrid nanofluids and their base lubricants to traditional nanofluids and their base lubricants, hybrid nanofluids generally offer higher thermal reliability. Enhancing the efficiency of thermal systems is crucial across sectors such as heat pumps, microelectronics, automotive radiators, heat capacitors, and vehicle power generation. Hybrid nanofluids are utilized in machine tool coolants, digital cooling systems, cancer treatments, nuclear energy facilities, chemical processing, nano-drug delivery, and more. Several articles provide insights into advancements in this field. For instance, Tian et al. [28] examined the effects of incorporating

multi-walled carbon nanotubes into engine oil as a base fluid, creating a hybrid suspension with two nanoparticles for use in advanced neural artificial applications. Bumataria et al. [29] analyzed hybrid nanofluids and their applications in heat pipe technology. Similarly, Yang et al. [30] provided a comprehensive review covering the uses of hybrid nanofluids, their properties, and fabrication methods for advanced cooling purposes. Khan et al. [31] examined the mixed convection flow utilizing a blend of Al_2O_3 and SiO_2 in water as the base fluid for various practical applications. Tlili et al. [32] focused on the microscopic exploration of magneto-hybrid nanofluids. Notably, the concept of tri-hybrid nanofluids has been advanced, demonstrating the simultaneous effects of three distinct nanoparticles in a single solution. This tri-hybrid mixture is receiving greater attention and demonstrates superior performance compared to traditional hybrid and nanofluids. The study of ternary-hybrid nanofluids has promising applications across different physical scenarios and is gaining traction in heat transfer challenges. Arif et al. [33] detailed the dispersion of diverse nanoparticles with varying shapes within water-based ternary-hybrid nanofluids for advanced thermal applications in radiators. Zeb et al. [34] studied the thermal dynamics and Casson fluid of ternary hybrid nanofluids, which are made up of Titanium Oxide (TiO_2), Aluminum Oxide (Al_2O_3), and Cobalt Ferrite ($CoFe_2O_3$) in water-based fluid that moves between two rotating disks. They consider the effects of quadratic heat radiation, magnetic fields, and mixed convection. Xuan et al. [35] conducted sensitivity analyses on tri-hybrid nano-liquids to further enhance thermal performance. Ahmad et al. [36] investigated the heat transfer capabilities of tri-hybrid nano-liquids in real-world applications. Adun et al. [37] described the synthesis methods for ternary-hybrid nano-liquids composed of a Fe_3O_4-Al_2O_3-ZnO mixture in water and analyzed the effects of volume concentration, temperature, and mixing ratios.

Here, we discussed how Soret/Dufour and combined convection affect Jeffrey, Maxwell, and micropolar nanofluid flow when temperature and concentration change. To illustrate how different emergent parameters affect the involved distributions, numerous graphics are created. The numerical results for the skin friction and the local Sherwood and Nusselt numbers are presented in tabular form and graphically.

Despite growing interest in nanofluids for thermal applications, most studies are limited to mono- or binary hybrid nanofluids and use Newtonian models. The dynamic interplay of Soret and Dufour effects in tri-hybrid nanofluids remains underexplored, particularly for non-Newtonian base fluids such as Jeffrey, Maxwell, and micropolar types. Furthermore, comparative studies incorporating these rheological models under identical parametric conditions are lacking. This work addresses this gap by modeling mixed convection over a porous surface using a tri-hybrid nanofluid composed of Multi-Walled Carbon Nanotubes (MWCNTs), Molydenium disulphide (MoS_2), and Graphene Oxide (GO), providing quantitative benchmarks for velocity, temperature, and concentration distributions under varying Deborah numbers, porosity, and mass transfer rates.

Lastly, the current research predominantly relies on integer-order partial differential equation methods, which are insufficient for addressing the complex behavior and memory effects associated with physical flows. Existing literature highlights that fractional-order differential operators, with their nonlocal properties, are well-suited to describing the global correlations within complex dynamic systems, phenomena, and structures [38–40]. Fractional calculus has proven effective in solving fluid flow challenges across various applications [41, 42]. Furthermore, the distribution of nanoscale particles in nanofluids demonstrates fractal characteristics. Recent studies suggest that fractional-order nanofluid models align significantly better with experimental data than their integer-order counterparts, establishing fractional nanofluid research as an emerging area of interest [43, 44]. Current advancements in fractional nanofluid modeling are being critically analyzed to deepen the understanding of key parameters influencing anomalous heat transfer and nanoparticle diffusion in thermal and flow control systems. In this work, we extend the classical model to a fractional framework, providing a more general and accurate representation of flow physics.

Novelty of the study:

This study is novel in simultaneously comparing Jeffrey, Maxwell, and micropolar non-Newtonian rheological models under identical mixed-convection conditions using a tri-hybrid nanofluid composed of MWCNT, MoS_2, and GO—an unexplored combination in prior literature. Unlike existing works focused on mono- or bi-hybrid nanofluids, the present framework incorporates Soret and Dufour effects, porous medium resistance, suction/injection, and variable thermal-solutal fields within a single unified model. A fractional-order formulation is introduced to capture memory-driven and nonlocal transport behaviors, offering a more generalized description than classical integer-order models. Quantitative

benchmarks for Nusselt, Sherwood, and skin-friction responses are provided for the first time for tri-hybrid non-Newtonian fluids, filling key gaps in comparative rheological analyses and providing a foundation for future optimization of advanced thermal systems.

Some main definitions:

Definition 1 The gamma function $\Gamma(x)$ is defined by the integral

$$\Gamma(x) = \int_0^\infty t^{x-1} e^{-t} dt, \quad x > 1.$$

And it satisfies the following functional equation

$$\Gamma(n+1) = n\Gamma(n) = n!\,, \quad \Gamma\left(\frac{1}{2}\right) = \sqrt{\pi}.$$

The limit gives the gamma function

$$\Gamma(x) = \lim_{n\to\infty} \frac{n! n^x}{x(x+1)(x+2)\ldots(x+n)}.$$

Definition 2 Caputo's fractional derivative is defined as:

$${}_a^C D_\tau^\alpha f(\tau) = \begin{cases} \dfrac{1}{\Gamma(\alpha-n)} \displaystyle\int_a^\tau \frac{f^{(n)}(t)dt}{(\tau-t)^{\alpha-n+1}}, & n-1 < \alpha < n, \quad n \in \mathbb{N}, \\ \dfrac{d^n f(\tau)}{d\tau^n}, & \alpha = n \in \mathbb{N}. \end{cases}$$

For $n = 1$ and lower terminal $a = 0$, the fractional derivative is

$${}_0^C D_t^\alpha f(\tau) = \frac{1}{\Gamma(\alpha-1)} \int_a^t \frac{f^{(')}(t)dt}{(\tau-t)^\alpha}, \quad 0 < \alpha < n.$$

Definition 3 Riemann-Liouville fractional derivative is given by:

$${}_a D_t^\alpha f(\tau) = \begin{cases} \dfrac{1}{\Gamma(\alpha-n)} \dfrac{d^n}{\tau^n} \displaystyle\int_a^\tau \frac{f(t)dt}{(\tau-t)^{\alpha-n+1}}, & n-1 < \alpha < n, \quad n \in \mathbb{N}, \\ \dfrac{d^n f(\tau)}{d\tau^n}, & \alpha = n \in \mathbb{N}. \end{cases}$$

2. Mathematical analysis

Given a vertical stretched surface (velocity $u_w(x)$), we consider a two-dimensional Jeffrey, Maxwell, and a micropolar tri-hybrid nanofluid flow across a porous medium with variable concentration $C_w(x)$, variable temperature $T_w(x)$, uniform

ambient concentration C_∞ and uniform ambient temperature T_∞. Additionally, we take into account the combined effects of Soret and Dufour in the presence of combined convection. Also taken into account are density variations and Buoyancy effects. For the concentration and temperature profiles, the Boussinesq approximation is used (see Figure 1). The suggested model's governing equations are [45, 46]:

$$u\frac{\partial u}{\partial x}+v\frac{\partial u}{\partial y}=\left(\frac{\mu_{thnf}+k}{\rho_{thnf}}\right)\left(\frac{1}{1+\lambda_2}\right)\left(\frac{\partial^2 u}{\partial y^2}+\lambda_3\left(u\frac{\partial^3 u}{\partial x\partial y^2}+\frac{\partial u}{\partial y}\frac{\partial^2 u}{\partial x\partial y}+v\frac{\partial^3 u}{\partial y^3}-\frac{\partial u}{\partial x}\frac{\partial^2 u}{\partial y^2}\right)\right)$$

$$+\frac{k}{\rho_{thnf}}\frac{\partial N}{\partial y}-\lambda_1\left[u^2\frac{\partial^2 u}{\partial x^2}+v^2\frac{\partial^2 u}{\partial y^2}+2uv\frac{\partial^2 u}{\partial x\partial y}\right]-\frac{\mu_{thnf}}{K\rho_{thnf}}u$$

$$+g^*\left[\frac{(\rho\beta_T)_{thnf}}{\rho_{thnf}}(T-T_\infty)+\frac{(\rho\beta_C)_{thnf}}{\rho_{thnf}}(C-C_\infty)\right]. \tag{1}$$

$$u\frac{\partial N}{\partial x}+v\frac{\partial N}{\partial y}=\frac{\gamma_{thnf}}{j\rho_{thnf}}\left(\frac{\partial^2 N}{\partial y^2}\right)-\frac{k}{j\rho_{thnf}}\left(2N+\frac{\partial u}{\partial y}\right). \tag{2}$$

$$u\frac{\partial T}{\partial x}+v\frac{\partial T}{\partial y}=\alpha^*_{thnf}\left[\frac{\partial^2 T}{\partial y^2}\right]+\frac{D_eK_T}{C_sC_p}\frac{\partial^2 C}{\partial y^2}+\tau\left[D_B\frac{\partial C}{\partial y}\frac{\partial T}{\partial y}+\frac{D_T}{T_\infty}\left(\frac{\partial T}{\partial y}\right)^2\right]. \tag{3}$$

$$u\frac{\partial C}{\partial x}+v\frac{\partial C}{\partial y}=D_B\left(\frac{\partial^2 C}{\partial y^2}\right)+\frac{D_eK_T}{T_m}\frac{\partial^2 T}{\partial y^2}+\frac{D_T}{T_\infty}\left(\frac{\partial^2 T}{\partial y^2}\right). \tag{4}$$

Given suitable boundary conditions:

$$u=u_w(x)=ax,\quad v=-v_0,\quad T=T_w(x)=T_\infty+bx,\quad N=0,\quad C=C_w(x)=C_\infty+cx\ \text{ at }\ y=0,$$

$$u\to 0,\quad \frac{\partial u}{\partial y}\to 0,\quad T\to T_\infty,\quad N\to 0,\quad C\to C_\infty\ \text{ as }\ y\to\infty. \tag{5}$$

Velocity components u and v are located along the x and y-axes in this case. Furthermore, T, N, C, D_B, D_T, g^*, α^*, λ_1, λ_2, λ_3, β_T, and $\tau=\frac{(\rho d)_p}{(\rho d)_f}$ are nanofluid temperature, angular velocity, nanofluid concentration, Brownian motion coefficient, thermophoretic diffusion coefficient, gravitation acceleration, thermic diffusivity, relaxation time, the relaxation to the radiation time ratio, retardation time, thermic expansion coefficient, and the fluid's effective heat capacity divided by the nanoparticle's. ρ_{thnf} refer to nanofluid density, μ_{thnf} is the nanofluid effective viscosity, $\gamma_{thnf}=\left(\mu_{thnf}+\frac{k}{2}\right)j=\mu_f\left(\frac{\mu_{thnf}}{\mu_f}+\frac{R}{2}\right)j$ is the spin gradient tri-hybrid nanofluid, $(\rho C_p)_{thnf}$ is nanofluid heat capacitance, k_{thnf} represent nanofluid thermal conductivity. Additionally, the constants $a>0$ and $c>0$ are positive. Nevertheless, $b>0$ indicates a heated plate ($T_w>T_\infty$), and the corresponding constant for a cooled surface ($T_w<T_\infty$), is $b<0$.

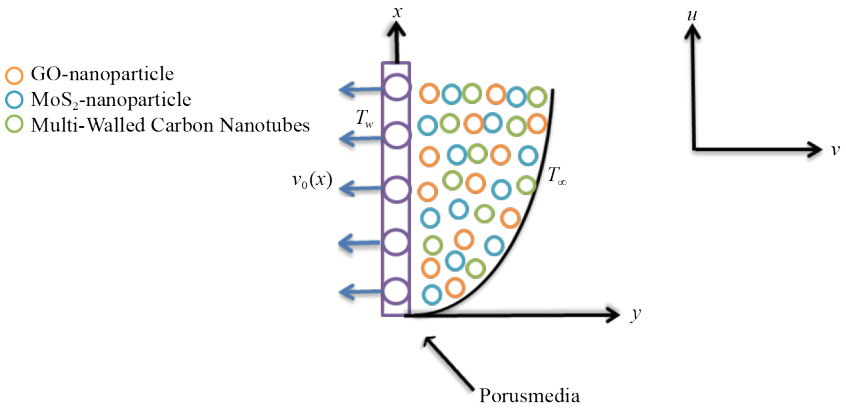


Figure 1. Physical problem

When a fractional coefficient of order α is applied to equations (1)-(4); the governing equations (6)-(9):

$$u\frac{\partial u}{\partial x}+v\frac{\partial u}{\partial y}=\left(\frac{\mu_{thnf}+k}{\rho_{thnf}}\right)\left(\frac{1}{1+\lambda_2}\right)\left(\frac{\partial^{\alpha+1}u}{\partial y^{\alpha+1}}+\lambda_3\left(u\frac{\partial^{\alpha+2}u}{\partial x^{\alpha}\partial y^{\alpha+1}}+\frac{\partial^{\alpha}u}{\partial y^{\alpha}}\frac{\partial^{\alpha+1}u}{\partial x^{\alpha}\partial y^{\alpha}}+v\frac{\partial^{\alpha+2}u}{\partial y^{\alpha+2}}-\frac{\partial^{\alpha}u}{\partial x^{\alpha}}\frac{\partial^{\alpha+1}u}{\partial y^{\alpha+1}}\right)\right)$$

$$-\lambda_1\left[u^2\frac{\partial^{\alpha+1}u}{\partial x^{\alpha+1}}+v^2\frac{\partial^{\alpha+1}u}{\partial y^{\alpha+1}}+2uv\frac{\partial^{\alpha+1}u}{\partial x^{\alpha}\partial y^{\alpha}}\right]-\frac{\mu_{thnf}}{K\rho_{thnf}}u$$

$$+g^*\left[\frac{(\rho\beta_T)_{thnf}}{\rho_{thnf}}(T-T_\infty)+\frac{(\rho\beta_C)_{thnf}}{\rho_{thnf}}(C-C_\infty)\right]. \tag{6}$$

$$u\frac{\partial N}{\partial x}+v\frac{\partial N}{\partial y}=\frac{\gamma_{thnf}}{j\rho_{thnf}}\left(\frac{\partial^{\alpha+1}N}{\partial y^{\alpha+1}}\right)-\frac{k}{j\rho_{thnf}}\left(2N+\frac{\partial^{\alpha}u}{\partial y^{\alpha}}\right). \tag{7}$$

$$u\frac{\partial T}{\partial x}+v\frac{\partial T}{\partial y}=\alpha^*\left[\frac{\partial^{\alpha+1}T}{\partial y^{\alpha+1}}\right]+\frac{D_eK_T}{C_sC_p}\frac{\partial^{\alpha+1}C}{\partial y^{\alpha+1}}+\tau\left[D_B\frac{\partial^{\alpha}C}{\partial y^{\alpha}}\frac{\partial^{\alpha}T}{\partial y^{\alpha}}+\frac{D_T}{T_\infty}\left(\frac{\partial^{\alpha}T}{\partial y^{\alpha}}\right)^2\right]. \tag{8}$$

$$u\frac{\partial C}{\partial x}+v\frac{\partial C}{\partial y}=D_B\left(\frac{\partial^{\alpha+1}C}{\partial y^{\alpha+1}}\right)+\frac{D_eK_T}{T_m}\frac{\partial^{\alpha+1}T}{\partial y^{\alpha+1}}+\frac{D_T}{T_\infty}\left(\frac{\partial^{\alpha+1}T}{\partial y^{\alpha+1}}\right). \tag{9}$$

The fractional partial differential equations described above can be transformed into fractional equations by using the similarity relations displayed below. The similarity variable's dimensionless functions f, g, θ, ϕ, and η [45, 53]:

$$\psi=x\sqrt{a\nu_f}f(\eta^\alpha),\quad N=\frac{du}{dy}=a\sqrt{\frac{a}{\nu_f}}xg(\eta^\alpha),\quad \theta(\eta^\alpha)=\frac{T-T_\infty}{T_w-T_\infty},$$

$$\phi(\eta^\alpha)=\frac{C-C_\infty}{C_w-C_\infty},\quad \eta^\alpha=\sqrt{\frac{a}{\nu_f}}\frac{y^\alpha}{\Gamma\alpha+1}. \tag{10}$$

Given that the stream function with $u = \frac{\partial \psi}{\partial y}$, $v = -\frac{\partial \psi}{\partial x}$ is $\psi(x, y)$, the fractional differential equations that can be obtained through some computation are as follows:

$$
\begin{aligned}
&(f^{\alpha})^2 + \frac{(\alpha-1)}{\alpha}\eta^{-\alpha} f f^{\alpha} - f f^{2\alpha} \\
&= \frac{\rho_f}{\rho_{thnf}}\left(\frac{\mu_{thnf}}{\mu_f} + R\right)\left(\frac{1}{1+\lambda_1}\right)\left[\frac{(\alpha-1)(\alpha-2)}{\alpha}\eta^{-\alpha-1} f^{\alpha} + 3(\alpha-1)\eta^{-\alpha} f^{2\alpha} + \alpha\eta^{-\alpha+1} f^{3\alpha}\right] \\
&+ \beta_2\left[2(\alpha-1)\eta^{-2}(f^{\alpha})^2 + 2\alpha\eta^{\alpha-2} f^{\alpha} f^{2\alpha} + \alpha^2\eta^{2\alpha-2}(f^{2\alpha})^2 - \frac{(\alpha-1)(\alpha-2)(\alpha-3)}{\alpha}\eta^{-\alpha-2} f f^{\alpha}\right. \\
&\left. - (\alpha-1)(7\alpha-11)\eta^{-2} f f^{2\alpha} - 6\alpha(\alpha-1)\eta^{\alpha-2} f f^{3\alpha} - \alpha^2\eta^{2\alpha-2} f f^{4\alpha}\right] \\
&- \gamma\frac{\mu_{thnf}}{\mu_f}\frac{\rho_f}{\rho_{thnf}}\frac{\eta^{-\alpha+1}}{\alpha} f^{\alpha} + \lambda\left(\frac{(\rho\beta_T)_{thnf}}{(\rho\beta_T)_f}\frac{\rho_f}{\rho_{thnf}}\theta + \frac{(\rho\beta_C)_{thnf}}{(\rho\beta_C)_f}\frac{\rho_f}{\rho_{thnf}} Nr\phi\right) \\
&- \beta\left[\frac{(\alpha-1)(\alpha-2)}{\alpha}\eta^{-\alpha-1} f^2 f^{\alpha} + 3(\alpha-1)\eta^{-1} f^2 f^{2\alpha} + \alpha\eta^{\alpha-1} f^2 f^{3\alpha}\right. \\
&\left. - 2(\alpha-1)\eta^{-1} f (f^{\alpha})^2 - 2\alpha\eta^{\alpha-1} f f^{\alpha} f^{2\alpha}\right] = 0. \qquad (11)
\end{aligned}
$$

$$
\begin{aligned}
&\frac{\rho_f}{\rho_{thnf}}\left(\frac{\mu_{thnf}}{\mu_f} + \frac{R}{2}\right)\left(\alpha\eta^{\alpha-1} g^{2\alpha} + (\alpha-1)\eta^{-1} g^{\alpha}\right) \\
&- \frac{\rho_f}{\rho_{thnf}} RB\left(\frac{2}{\alpha}\eta^{-\alpha+1} g + (\alpha-1)\eta^{-1} f^{\alpha} + \alpha\eta^{\alpha-1} f^{2\alpha}\right) = \alpha\eta^{\alpha-1}(g f^{\alpha} - f g^{\alpha}). \qquad (12)
\end{aligned}
$$

$$
\begin{aligned}
&\frac{k_{thnf}}{k_f}\frac{(\rho c_p)_f}{(\rho c_p)_{thnf}}\frac{1}{\mathrm{Pr}}\left[(\alpha-1)\eta^{-1}\theta^{\alpha} + \alpha\eta^{\alpha-1}\theta^{2\alpha}\right] + D_f\alpha\eta^{\alpha-1}\phi^{2\alpha} \\
&+ D_f(\alpha-1)\eta^{-1}\phi^{\alpha} + Df\alpha\eta^{\alpha-1}\phi^{2\alpha} + Nb\alpha\eta^{\alpha-1}\theta^{\alpha}\phi^{\alpha} \\
&+ Nt\alpha\eta^{\alpha-1}(\theta^{\alpha})^2 + f\theta^{\alpha} - \theta f^{\alpha} + 0. \qquad (13)
\end{aligned}
$$

$$
\phi^{2\alpha} + \mathrm{Pr}Le\,\frac{\eta^{1-\alpha}}{\alpha}(f\phi^{\alpha} - \phi f^{\alpha}) + S_r Le\theta^{2\alpha} + \frac{Nt}{Nb}\theta^{2\alpha} + \frac{(\alpha-1)}{\alpha\eta}\phi^{\alpha} + SrLe\frac{(\alpha-1)}{\alpha\eta}\theta^{\alpha} = 0\,. \qquad (14)
$$

Entering the fractional order ($\alpha = 1$) causes the fractional equations and transformations to convert into their non-fractional form:

$$(f')^2 - ff'' = \frac{\rho_f}{\rho_{thnf}}\left(\frac{\mu_{thnf}}{\mu_f} + R\right)\left(\frac{1}{1+\lambda_1}\right)\left[f''' + \lambda_4\left(f''^2 - ff^{iv}\right)\right] - \gamma\frac{\mu_{thnf}}{\mu_f}\frac{\rho_f}{\rho_{thnf}}f'$$

$$+\lambda\left(\frac{(\rho\beta_T)_{thnf}}{(\rho\beta_T)_f}\frac{\rho_f}{\rho_{thnf}}\theta + \frac{(\rho\beta_C)_{thnf}}{(\rho\beta_C)_f}\frac{\rho_f}{\rho_{thnf}}Nr\phi\right) + \frac{\rho_f}{\rho_{thnf}}Rg' - \beta(f^2 f''' - 2ff'f''). \tag{15}$$

$$\frac{\rho_f}{\rho_{thnf}}\left(\frac{\mu_{thnf}}{\mu_f} + \frac{R}{2}\right)g'' - \frac{\rho_f}{\rho_{thnf}}RB\left(2g + f''\right) - gf' + fg' = 0. \tag{16}$$

$$\frac{k_{thnf}}{k_f}\frac{(\rho c_p)_f}{(\rho c_p)_{thnf}}\frac{1}{\Pr}\theta'' + Df\phi'' + Nb\theta'\phi' + N_t\theta'^2 - \theta f' + f\theta' = 0. \tag{17}$$

$$\phi'' + \Pr Le\left(f\phi' - \phi f'\right) + SrLe\theta'' + \frac{N_t}{N_b}\theta'' = 0. \tag{18}$$

For,

$$f(0) = S, \quad f'(0) = 1, \quad \theta(0) = 1, \quad g(0) = 0, \quad \phi(0) = 1,$$

$$f'(\infty) \to 0, \quad f'' \to 0, \quad \theta(\eta) \to 0, \quad g(\eta) \to 0, \quad \phi(\eta) \to 0, \quad \text{as} \quad \eta \to \infty. \tag{19}$$

Since $\alpha^*_{thnf} = \dfrac{k_{thnf}}{(\rho c_p)_{thnf}}$ is the thermal diffusivity, $Nt = \dfrac{\tau D_T(T_w - T_\infty)}{\nu_f T_\infty}$ thermophoresis parameter, $Nb = \dfrac{\tau D_B(C_w - C_\infty)}{\nu_f}$ is the Brownian motion parameter, $Le = \dfrac{k_f}{D_B(\rho c_p)_f}$, $\lambda_4 = a\lambda_3$, $\Pr = \dfrac{\nu_f}{\alpha_f}$, $(\beta \geq 0) = a\lambda_1$, $\lambda = \dfrac{Gr_x}{{Re_x}^2}$, $Nr = \dfrac{\beta_c(C_w - C_\infty)}{\beta_T(T_w - T_\infty)}$, $\gamma = \dfrac{\nu_f}{aK}$, $Sr = \dfrac{D_e K_T(T_w - T_\infty)}{T_m\alpha_f}$, $Df = \dfrac{D_e K_T(C_w - C_\infty)}{C_s C_p(T_w - T_\infty)}$ and $R = \dfrac{k}{\mu_f}$, $B = \dfrac{\mu_f}{ja\rho_f}$ are respectively Lewis number, Deborah number with respect to retardation time, Prandtl number, the Deborah number with respect to relaxation time, combined convection parameter, the concentration buoyancy parameter, porosity parameter, the Soret number, the Dufour number, and material parameters. Moreover, $Re_x = \dfrac{xu_w}{\nu_f}$ is the Reynolds number and $Gr_x = \dfrac{g^*\beta_T(T_w - T_\infty)x^3}{\nu_f^2}$ is the Grashof number. Additionally, ($\lambda < 0$, $\lambda = 0$, and $\lambda > 0$) represent opposing flow (cooled plate), forced convective flow, and supportive flow (hot plate). Furthermore, when $Nr = 0$ (without mass transport), Nr might have both positive ($Nr > 0$) and negative ($Nr < 0$) values.

Also significant and need to be considered are the Skin friction coefficient C_f, the Sherwood number Sh, and the Nusselt number Nu_x, which

$$\tau_w = \mu_{thnf}\frac{\left(1 + \frac{R}{2} + \beta\right)}{(1+\lambda_4)}\frac{\partial u}{\partial y}\Big|_{y=0}, \quad q_m = -D_B\frac{\partial C}{\partial y}\Big|_{y=0}, \quad q_w = -k_{thnf}\frac{\partial T}{\partial y}\Big|_{y=0}, \tag{20}$$

where, τ_w is shear stress, q_m is mass flux, and q_w is heat flux. By using the dimensionless variables Eq. (10) with $\alpha = 1$, and 20, then

$$Re_x^{\frac{1}{2}} C_f = \frac{\mu_{thnf}}{\mu_f} \frac{\left(1 + \frac{R}{2} + \beta\right)}{(1+\lambda_4)} f''(0), \quad Re_x^{-\frac{1}{2}} Nu_x = -\frac{k_{thnf}}{k_f} \theta'(0), \quad Re_x^{-\frac{1}{2}} Sh = -\phi'(0). \tag{21}$$

3. Thermophysical properties

The thermophysical properties of the ternary hybrid nanofluid, essential for modeling its enhanced behavior, are determined using established effective-medium theory correlations. These relations, which calculate the effective density, dynamic viscosity, heat capacity, thermal conductivity, and electrical conductivity based on the respective volume fractions of the dispersed nanoparticles (MoS_2, GO, and MWCNT), are comprehensively summarized in Table 1 [47–49]. The requisite numerical values for the base fluid (water) and the individual nanoparticle materials used in these correlations are provided in Table 2 [50, 51]. Employing these models is critical for accurately capturing the significant alterations in the fluid's transport characteristics imparted by the nanoparticle dispersion.

Table 1. Tri-hybrid nanofluid's thermo-physical characteristics can be summed up as [47–49]

Base fluid	Water (H_2O)
Nanoparticles	$\phi_1 = \phi_{MoS_2}, \phi_2 = \phi_{GO}, \phi_3 = \phi_{MWCNT},$ $\phi_{nf} = \phi_1, \phi_{hnf} = \phi_1 + \phi_2, \phi_{thnf} = \phi_1 + \phi_2 + \phi_3.$
Viscosity	$\mu_{nf} = \frac{\mu_f}{(1-\phi_1)^{2.5}}, \mu_{hnf} = \frac{\mu_f}{(1-\phi_1)^{2.5}(1-\phi_2)^{2.5}}, \mu_{thnf} = \frac{\mu_f}{(1-\phi_1)^{2.5}(1-\phi_2)^{2.5}(1-\phi_3)^{2.5}}.$
Density	$\frac{\rho_{nf}}{\rho_f} = (1-\phi_1) + \phi_1 \frac{\rho_1}{\rho_f}, \frac{\rho_{hnf}}{\rho_f} = (1-\phi_2)\left(\phi_1\left(\frac{\rho_1}{\rho_f}\right) + (1-\phi_1)\right) + \phi_2 \frac{\rho_2}{\rho_f},$ $\frac{\rho_{thnf}}{\rho_f} = (1-\phi_1)\left(\phi_2\left(\frac{\rho_2}{\rho_f}\right) + (1-\phi_2)\left\{(1-\phi_3) + \phi_3 \frac{\rho_3}{\rho_f}\right\}\right) + \phi_1 \frac{\rho_1}{\rho_f}.$
Electrical conductivity	$\sigma_{nf1} = \frac{(1+2\phi_1)\sigma_1 + (1-2\phi_1)\sigma_{hnf}}{(1-\phi_1)\sigma_1 + (1+\phi_1)\sigma_{hnf}}, \sigma_{nf2} = \frac{(1+2\phi_2)\sigma_2 + (1-2\phi_2)\sigma_{nf}}{(1-\phi_2)\sigma_2 + (1+\phi_2)\sigma_{nf}}, \sigma_{nf3} = \frac{(1+2\phi_3)\sigma_3 + (1-2\phi_3)\sigma_f}{(1-\phi_3)\sigma_3 + (1+\phi_3)\sigma_f},$ $\frac{\sigma_{nf}}{\sigma_f} = \frac{\sigma_{nf1}\phi_1}{\phi_{nf}}, \frac{\sigma_{hnf}}{\sigma_f} = \frac{\sigma_{nf1}\phi_1 + \sigma_{nf2}\phi_2}{\phi_{hnf}}, \frac{\sigma_{thnf}}{\sigma_f} = \frac{\sigma_{nf1}\phi_1 + \sigma_{nf2}\phi_2 + \sigma_{nf3}\phi_3}{\phi_{thnf}}.$
Thermic conductivity	$k_{nf1} = \frac{k_1 + 2k_f - 2\phi_1(k_f - k_1)}{k_1 + 2k_f + \phi_1(k_f - k_1)}, k_{nf2} = \frac{k_2 + 2k_{nf1} - 2\phi_2(k_{nf1} - k_2)}{k_2 + 2k_{nf1} + \phi_2(k_{nf1} - k_2)}, k_{nf3} = \frac{k_3 + 2k_{nf2} - 2\phi_3(k_{nf2} - k_3)}{k_3 + 2k_{nf2} + \phi_3(k_{nf2} - k_3)},$ $\frac{k_{nf}}{k_f} = \frac{k_{nf1}\phi_1}{\phi_{nf}}, \frac{k_{hnf}}{k_f} = \frac{k_{nf1}\phi_1 + k_{nf2}\phi_2}{\phi_{hnf}}, \frac{k_{thnf}}{k_f} = \frac{k_{nf1}\phi_1 + k_{nf2}\phi_2 + k_{nf3}\phi_3}{\phi_{thnf}}.$
Heat capacity	$(\rho C_p)_{nf1} = (1-\phi_1) + \frac{(\rho C_p)_1}{(\rho C_p)_f}\phi_1, (\rho C_p)_{nf2} = (1-\phi_2) + \frac{(\rho C_p)_2}{(\rho C_p)_f}\phi_2, (\rho C_p)_{nf3} = (1-\phi_3) + \frac{(\rho C_p)_3}{(\rho C_p)_f}\phi_3,$ $\frac{(\rho C_p)_{nf}}{(\rho C_p)_f} = (\rho C_p)_{nf1}, \frac{(\rho C_p)_{hnf}}{(\rho C_p)_f} = (\rho C_p)_{nf1} + (\rho C_p)_{nf2}, \frac{(\rho C_p)_{hnf}}{(\rho C_p)_f} = (\rho C_p)_{nf1} + (\rho C_p)_{nf2} + (\rho C_p)_{nf3}.$

Table 2. Thermophysical chracteristics of the nanoparticle and regular fluid [50, 51]

Physical properties	Water (H_2O)	Molydenium disulphide (MoS_2)	Graphene Oxide (GO)	Multi-walled carbon nanotubes
$\rho\left(\frac{Kg}{m^3}\right)$	997.1	5,060	2,200	1,600
$k\left(\frac{W}{m}\cdot K\right)$	0.613	904.4	5,000	3,000
$C_p\left(\frac{J}{Kg}\cdot K\right)$	4,179	397.21	790	796
$\sigma\left(\frac{S}{m}\right)$	0.005	2.09×10^{4}	6.30×10^{7}	1.90×10^{-4}
$\beta\times10^{5}\left(\frac{1}{K}\right)$	-	2.84×10^{-5}	2.84×10^{-4}	44
Pr	6.8	-	-	-

3.1 *Model validation*

Tables 3-6 are validation tables. To ensure the accuracy of our numerical method, we compared our results with established literature for simplified cases. For Newtonian fluids, our local Nusselt number results align perfectly with prior studies, showing a maximum difference of only 0.47%. Validation of Maxwell fluids against skin-friction and Nusselt-number data also showed strong agreement, with differences remaining below 0.73% for one set of parameters and 1.20% for another. A final comprehensive check against data for skin friction, Nusselt, and Sherwood numbers confirmed the robustness of our approach, with a maximum deviation of 1.82%. These consistently small percentage differences across all validated parameters and outputs provide high confidence in the reliability of our present computational results.

Table 3. Comparison of $-\theta'(0)$ for Newtonian fluids when λ, Df, Sr, Nb, $Nt=0$, $Le=1$

S	Pr	[53]	[54]	[52]	Present results
	0.72	0.4570	0.4570	0.4570	0.4570
-1.5	1	0.5000	0.5000	0.5000	0.5000
	10	0.6542	0.6452	0.6452	0.6482
	0.72	0.8086	0.8086	0.8086	0.8086
0	1	1.0000	1.0000	1.0000	1.0000
	3	1.9237	1.9236	1.9359	1.9277
	0.72	1.4944	1.4944	1.4944	1.4944
1.5	1	2.0000	2.0001	2.0001	2.0000
	10	16.0842	16.0962	16.0962	16.0922

Table 4. Comparison of $-\theta'(0)$ and $-\phi'(0)$ for Maxwell fluids when $Df = 0.1$, $Le = 1$, $Sr = 0.2$, $Nb = 0.8$, $Nt = 0.1$ are fixed

Parameters		[55]		Present results	
		$-\theta'(0)$	$-\phi'(0)$	$-\theta'(0)$	$-\phi'(0)$
S	0	0.71104	0.89301	0.71093	0.89331
	0.3	0.79696	1.01679	0.79682	1.01691
	0.5	0.85983	1.10661	0.85983	1.10691
	0.9	0.99873	1.30359	0.99870	1.30352
β	0	0.8669	1.11816	0.86691	1.11820
	0.2	0.85263	1.09559	0.85263	1.09567
	0.4	0.83795	1.07326	0.83688	1.08382
γ	0.5	0.91493	1.19556	0.91402	1.19901
	1.0	0.89498	1.16286	0.89495	1.16290
	1.5	0.8768	1.13337	0.87656	1.13339
λ	0.5	0.81772	1.03883	0.81767	1.03910
	0.8	0.84445	1.08202	0.84444	1.08231
	1.2	0.87379	1.12906	0.87380	1.12909
Nr	-0.2	0.80842	1.02316	0.80841	1.02341
	-0.1	0.81357	1.03149	0.81355	1.03186
	0.5	0.84071	1.07596	0.84070	1.07611
Pr	0.7	0.77431	0.84566	0.77418	0.84612
	1.2	0.88622	1.27852	0.88620	1.27851
	1.5	0.89045	1.53416	0.89044	1.53414

Table 5. Comparison of $-\theta'(0)$ and $-\phi'(0)$ for Maxwell fluids when $S = 0.5$, $\beta = 0.1$, $\gamma = 2.0$, $Nr = 1$, $\Pr = 1.0$ are fixed

Parameters		[54]		Present results	
		$-\theta'(0)$	$-\phi'(0)$	$-\theta'(0)$	$-\phi'(0)$
Df	0	0.92430	1.08556	0.92429	1.08561
	0.2	0.79244	1.12890	0.79246	1.12898
	0.4	0.64798	1.17570	0.64796	1.17575
Le	0.7	0.93603	0.82755	0.93589	0.82789
	1.2	0.81957	1.28184	0.81936	1.28186
	1.5	0.76852	1.53285	0.76850	1.53279
Sr	0	0.82745	1.21843	0.82745	1.21850
	0.2	0.84341	1.16386	0.84341	1.16392
	0.4	0.89416	0.98468	0.89421	0.98484
Nb	0.3	0.95038	0.77806	0.95038	0.77806
	0.5	1.07399	0.89003	1.07398	0.89016
	1	0.97908	1.02149	0.97910	1.02156
Nt	0	0.78921	1.14098	0.78920	1.14104
	0.3	0.87116	1.17100	0.87109	1.17112
	0.5	0.83699	0.98765	0.83693	0.98783
	0.5	0.81388	0.88051	0.81376	0.88083

Table 6. Comparison of skin friction, heat, and mass transfer rates for Maxwell fluids when $\lambda_4 = \lambda_1 = Nb = Nt$ are fixed

Parameters		[56]			Present results		
		$f''(0)$	$-\theta'(0)$	$-\phi'(0)$	$f''(0)$	$-\theta'(0)$	$-\phi'(0)$
β	0	1.4148	0.8658	0.8034	1.41496	0.86588	0.80347
	0.2	1.2949	0.8865	0.8235	1.30645	0.88659	0.82356
	0.4	1.2065	0.9031	0.8397	1.22038	0.9031	0.8397
γ	0	0.7466	1.0023	0.9380	0.61399	1.00236	0.93807
	1	1.0298	0.9417	0.8779	1.03054	0.94178	0.8779
	2	1.3498	0.8768	0.8141	1.35733	0.87683	0.81417
λ	0	1.3484	0.8552	0.7916	1.34846	0.85526	0.79165
	1	1.0298	0.9417	0.8779	1.03054	0.94167	0.87794
	2	0.7524	0.9938	0.9291	0.74370	0.99468	0.93004
Nr	-0.5	1.1261	0.7478	0.6759	1.13119	0.74445	0.67704
	-0.2	1.1568	1.0107	0.9546	1.15803	1.01063	0.95458
Pr	0.7	1.1742	1.2152	1.1899	1.17358	1.21530	1.19003
	1.2	1.1205	0.8155	0.8805	1.12598	0.81522	0.88012
	1.7	1.0951	0.7104	0.9103	1.10309	0.70994	0.90951
Df	0.3	1.0701	0.5975	0.9398	1.08034	0.59704	0.93872
	0.5	1.1344	0.9976	0.9604	1.13818	0.91145	0.96005
	0.7	1.1202	0.9070	1.1083	1.12521	0.90656	1.10762
Le	1.2	1.1126	0.9031	1.1981	1.11819	0.90255	1.19734
	1.5	1.1126	0.9031	1.1981	1.11819	0.90255	1.19734
	1.7	1.1297	0.9092	1.0174	1.13380	0.90886	1.01704
Sr	0.2	1.1475	0.9154	0.8278	1.15004	0.91533	0.82781
	0.4	1.4148	0.8658	0.8034	1.41496	0.94167	0.87794
	0.6	1.2949	0.8865	0.8235	1.2956	0.99468	0.93004

3.2 *Numerical solution procedure*

The system of coupled, nonlinear ordinary differential equations (15)-(18), subject to the boundary conditions (19), constitutes a two-point boundary value problem. Due to its strong nonlinearity and coupling, an analytical solution is intractable. Consequently, a numerical solution is obtained using the **bvp4c** solver in MATLAB, which is based on a finite difference code that implements the three-stage Lobatto IIIa formula.

The solution methodology is implemented as follows:

1. **Reduction of Ordinary Differential Equations (ODEs):** The higher-order system is transformed into a system of ten first-order ordinary differential equations by introducing new variables:

- $y_1 = f, y_2 = f', y_3 = f'', y_4 = f'''$;
- $y_5 = g, y_6 = g'$;
- $y_7 = \theta, y_8 = \theta'$;
- $y_9 = \phi, y_{10} = \phi'$.

2. **Implementation in solver:** The derived system of first-order equations is coded into a function file for the solver. A separate function file is created to specify the boundary conditions at $\eta = 0$ and as $\eta \to \infty$.

3. **Initial guess and mesh selection:** An appropriate initial guess, which satisfies the far-field boundary conditions asymptotically, is required for the iterative solver. A finite value approximates the infinite domain $[0, \infty)$ $\eta_{\max}$. Through numerical experimentation, $\eta_{\max} = 8$ was found to be sufficient to capture the asymptotic behavior of all profiles for all considered parametric values.

4. **Convergence criteria:** The computation is carried out with a relative error tolerance of 10^{-3} to ensure accurate convergence. The solver adaptively refines the mesh until the solution satisfies the specified tolerance and boundary conditions.

5. **Validation:** The credibility of the present numerical code is established by comparing its results for limiting cases with previously published works, as detailed in the Model Validation section (Tables 3-6). The excellent agreement confirms the validity of our computational procedure.

4. Results and discussion

The results section presents a systematic evaluation of how various dimensionless parameters affect velocity, angular velocity, temperature, and concentration distributions for Jeffrey, Maxwell, and micropolar tri-hybrid nanofluids. Using figures and comparative analyses, the influence of parameters such as Deborah numbers, Soret/Dufour effects, porosity, and flow type (suction/injection, assisting/opposing) is explored.

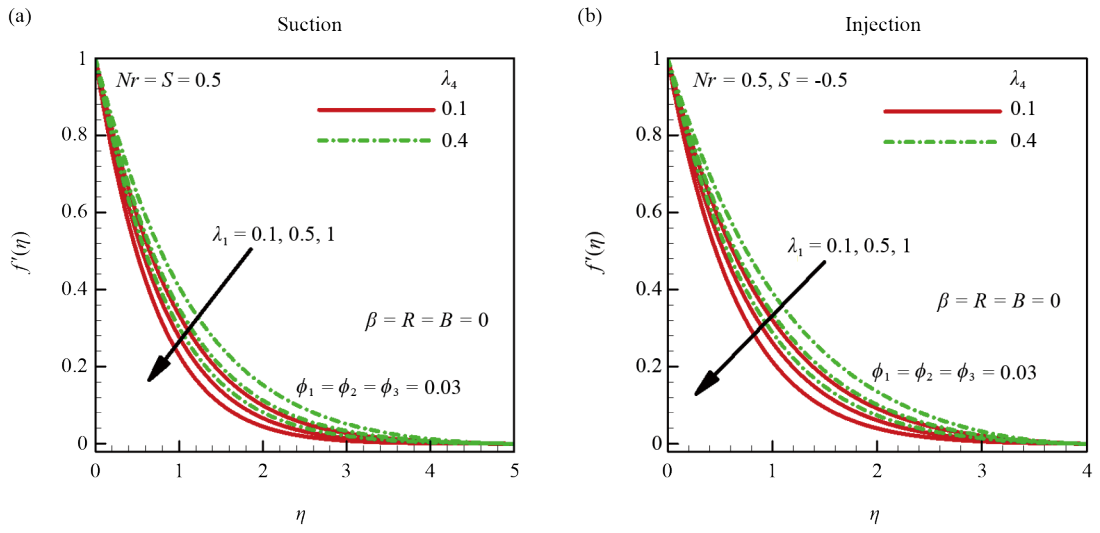


Figure 2. Dimensionless velocity profiles in Jeffrey ternary nanofluids, displaying the effects of Deborah numbers with respect to retardation and relaxation times

In Figure 2a, the dimensionless velocity profile $f'(\eta)$ is depicted for the suction case, where $S = 0.5$. The plots demonstrate how the velocity varies under different values of the Deborah numbers λ_1 (associated with relaxation time)

and λ_4 (associated with retardation time) in a Jeffrey ternary nanofluid system. Increasing λ_4 (green dash-dotted lines), which represents stronger retardation effects, leads to an increase in the velocity profile. This is because higher retardation weakens the fluid's elastic memory, allowing it to flow more freely. In contrast, increasing λ_1 (solid lines with increasing thickness) leads to a reduction in velocity due to enhanced relaxation behaviour—representing the fluid's tendency to resist deformation—thus slowing the motion. Under suction, the fluid is drawn toward the surface, leading to a thicker boundary layer, as the suction effect pulls more fluid from the external flow into the boundary layer, enhancing momentum diffusion.

In Figure 2b, the injection case is shown with $S = -0.5$. The trends remain consistent: increasing λ_4 promotes higher velocity, while increasing λ_1 suppresses it. Injection implies fluid is pushed from the surface into the domain, which tends to oppose the development of the boundary layer, resulting in a thinner velocity boundary layer. The injection action effectively displaces the outer fluid away from the wall, thereby diminishing the wall-adjacent flow region and reducing the boundary layer thickness.

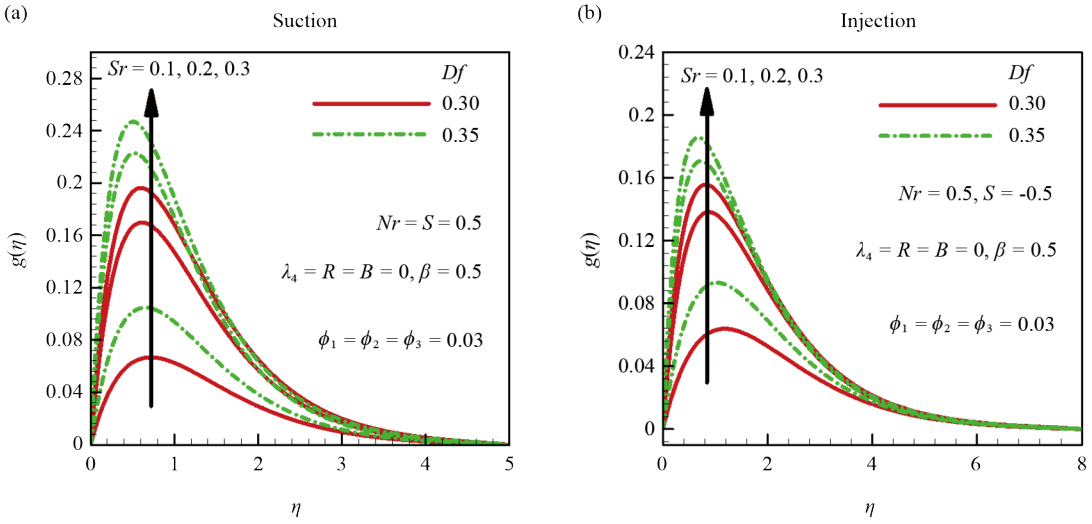


Figure 3. Dimensionless angular velocity profiles in Maxwell ternary nanofluids, displaying the effects of Soret and Deborah numbers

In Figure 3a, the dimensionless angular velocity profile $g(\eta)$ is analyzed for the suction case in Maxwell ternary nanofluids. The plot displays the effect of the Soret number (Sr)-which characterizes thermo-diffusion, i.e., the mass flux induced by a temperature gradient-and the Dufour number (Df)-which quantifies the energy flux due to concentration gradients. The red solid and green dash-dotted lines represent two different Dufour numbers (0.30 and 0.35, respectively), and the increasing line height indicates an increasing Soret number from 0.1 to 0.3. As both Sr and Df increase, there is a noticeable rise in the angular velocity peak near the wall. This behavior arises from enhanced cross-diffusion coupling: temperature gradients drive mass transport (Soret effect), and solute concentration gradients feed back energy into the system (Dufour effect), thereby collectively intensifying the angular motion near the wall. However, as η increases, $g(\eta)$ declines due to viscous damping and momentum diffusion overpowering the localized thermo-diffusion forces, leading to decay of angular motion in the outer boundary region. In suction, more fluid is pulled into the boundary layer, thickening it and allowing greater angular transport over a wider range.

In Figure 3b, the injection case is illustrated under similar parametric variation. As in the suction scenario, increasing Soret and Dufour numbers enhances the peak angular velocity near the surface. The Maxwell fluid's memory effects, combined with strong thermo-solutal interactions, stimulate rotation close to the wall. However, injection—by pushing fluid away from the surface-compresses the angular motion zone, leading to a thinner effective boundary layer and earlier decay of $g(\eta)$. The angular velocity still shows a peak due to near-wall momentum exchange, but attenuates more rapidly than in the suction case. The boundary layer in injection appears thinner because injection impedes the inward penetration

of momentum and suppresses the spread of rotational effects away from the wall. Thus, although the angular momentum initiates more sharply, it decays faster due to outward momentum flux and lower fluid retention near the boundary.

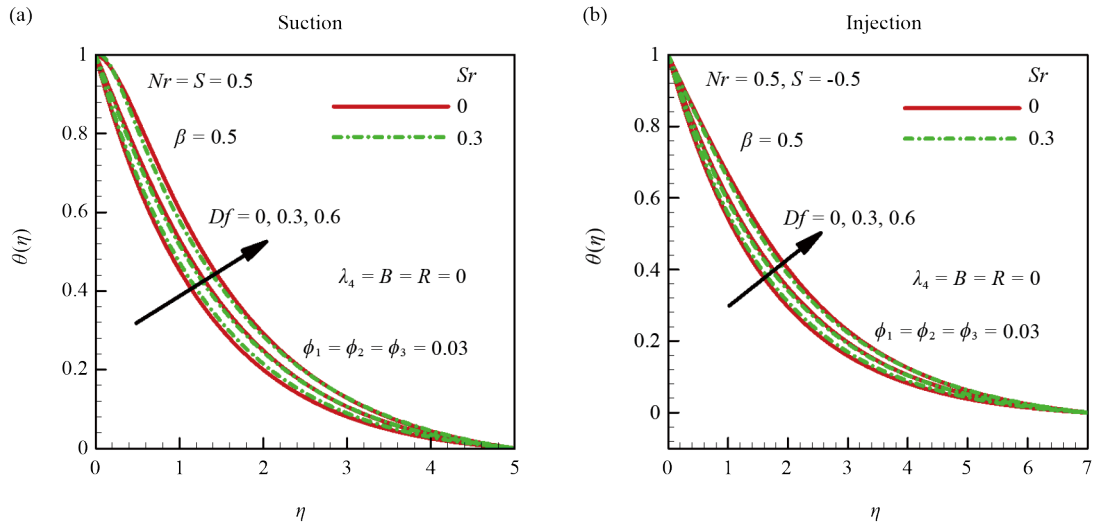


Figure 4. Dimensionless temperature profiles in Maxwell ternary nanofluids, showing the effects of Soret and Deborah numbers

In Figure 4a, the suction case is considered for Maxwell ternary nanofluids, where the variation of the dimensionless temperature profile $\theta(\eta)$ is presented. The Dufour number (Df) represents the effect of concentration gradients on heat transfer, introducing an additional thermal energy flux, while the Soret number (Sr) quantifies the influence of temperature gradients on mass diffusion. With increasing Dufour number (from 0 to 0.6) and non-zero Soret number (green dash-dotted curves), the thermal energy within the boundary layer intensifies, leading to a higher temperature profile. This occurs because the Dufour effect contributes to heat generation through solutal diffusion, and the Soret effect enhances thermal coupling via mass transport, thereby amplifying energy within the fluid. Despite this enhancement, suction draws cooler fluid toward the surface and suppresses the outward diffusion of heat, thereby reducing the thickness of the thermal boundary layer.

In Figure 4b, the injection case shows similar trends: increasing Soret and Dufour numbers lead to a rise in the temperature profile throughout the thermal boundary layer. The thermo-diffusive effects of these parameters intensify heat transport in the fluid. However, under injection (negative S), warm fluid is pushed away from the surface, allowing for greater thermal dispersion. This promotes a thicker thermal boundary layer than in the suction scenario, as the injected momentum enhances outward thermal diffusion and reduces heat retention near the wall. Therefore, the combination of Maxwell fluid relaxation effects and ternary nanofluid thermal properties results in a broader temperature spread in the injection case.

In Figure 5a, the assisting flow case is illustrated for Jeffrey ternary nanofluids, where buoyancy and free stream velocities act in the same direction ($Nr = S = 0.5$). This alignment promotes faster convective transport, leading to a thinner thermal boundary layer. As seen, increasing Soret (Sr) and Dufour (Df) numbers—representing cross-coupled mass and heat diffusion-causes an increase in the dimensionless temperature $\theta(\eta)$. These effects enhance energy transport via solutal diffusion and mass migration driven by thermal gradients, resulting in higher local surface temperatures. However, at lower Sr and Df, the thermodiffusive coupling is weakened, leading to heat conduction dominance and reduced temperature profiles. The assisting nature of the flow rapidly convects heat away from the surface, limiting the thickness of the thermal boundary layer.

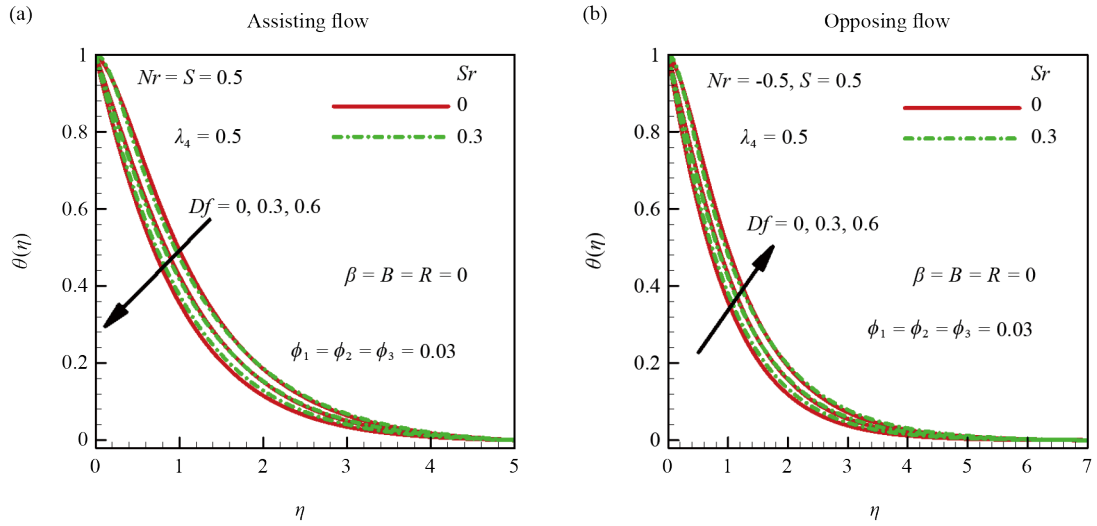


Figure 5. Dimensionless temperature profiles in Jaffrey ternary nanofluids, showing the effects of Soret and Deborah numbers

In Figure 5b, the opposing flow case is considered where $Nr = -0.5$ and $S = 0.5$, indicating that buoyancy and the external stream oppose each other. This resistance slows convective transport, allowing heat to accumulate near the wall and thereby thickening the thermal boundary layer. In this condition, the effects of increasing Soret and Dufour numbers become even more pronounced. Elevated Sr enhances mass diffusion due to thermal gradients, while a higher Df contributes additional heat flux due to solute concentration differences. This dual effect leads to greater temperature retention within the fluid. In contrast, when these numbers are lower, less thermal enhancement occurs, causing a drop in the temperature profile. The opposing flow delays thermal dissipation, resulting in a thicker boundary layer than in the assisting case.

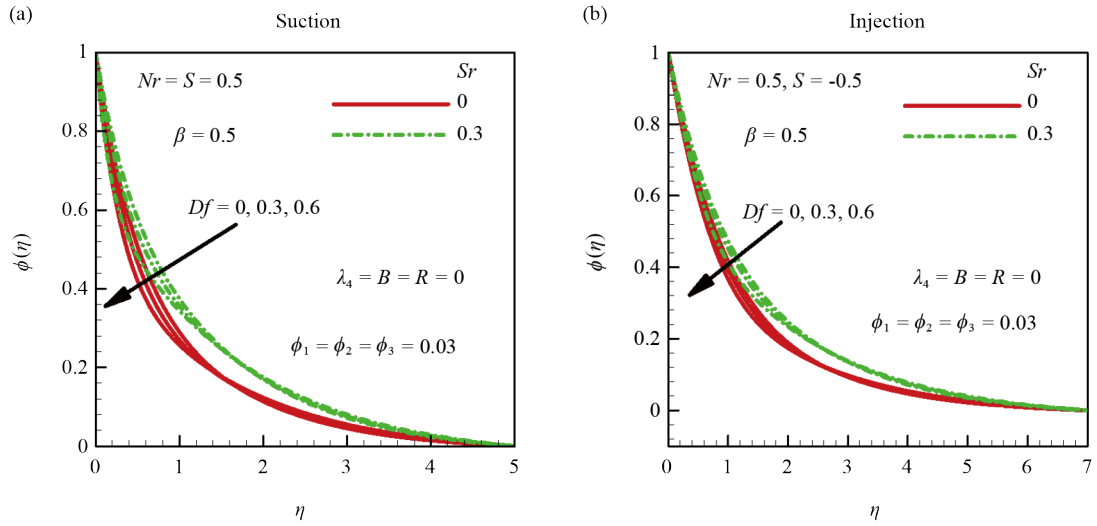


Figure 6. Dimensionless concentration profiles in Maxwell ternary nanofluids, showing the effects of Soret and Deborah numbers

In Figure 6a, the dimensionless concentration profile $\phi(\eta)$ is examined for in Maxwell ternary nanofluids. Suction pulls fluid toward the surface, compressing the solutal boundary layer and restricting mass diffusion, resulting in a thinner concentration boundary layer. The effects of Soret (Sr) and Dufour (Df) numbers are clearly illustrated: as

Df increases, the contribution of solutal diffusion to energy transport enhances, resulting in a higher concentration near the wall. However, increasing Sr (green dash-dotted lines) drives mass away from the surface due to thermal gradients, which lowers the concentration profile in the fluid. Conversely, lower Df reduces the thermally induced mass flux, further reducing the concentration across the boundary layer.

In Figure 6b, the injection case is presented where fluid is pushed outward from the surface into the boundary layer. This action encourages solutal spreading and leads to a thicker concentration boundary layer compared to suction. The same parametric trends are observed: higher Dufour numbers elevate the dimensionless concentration due to increased energy-induced mass diffusion. In comparison, higher Soret numbers reduce it by enhancing thermally driven mass dispersion away from the surface. Overall, the interaction of Sr and Df governs the balance between localized accumulation and outward migration of species. Injection facilitates a broader spatial distribution of nanoparticles, accounting for the increased boundary layer thickness in this case.

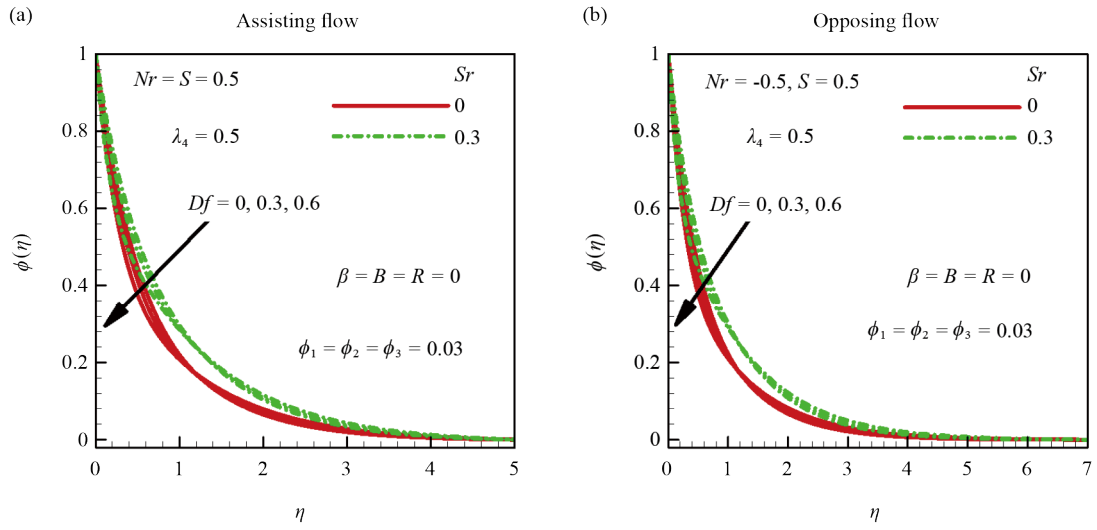


Figure 7. Dimensionless concentration profiles in Jaffrey ternary nanofluids, showing the effects of Soret and Deborah numbers

In Figure 7a, the assisting flow case is considered for Jeffrey ternary nanofluids. The dimensionless concentration profile $\phi(\eta)$ displays similar behavior to Jeffrey fluids—concentration increases with Dufour number due to enhanced mass diffusion driven by energy flux and decreases with higher Soret number as temperature gradients promote outward mass transport. The assisting flow condition ($Nr = S = 0.5$) aids the convective motion, reducing the thickness of the concentration boundary layer as thermal and solutal buoyancies align. This supports the sharper decay in concentration profile observed. The profile shapes remain consistent with those seen in Maxwell fluids due to similar physical mechanisms of Soret and Dufour coupling, although subtle distinctions arise from the rheological model.

In Figure 7b, the opposing flow case ($Nr = -0.5$, $S = 0.5$) is shown. The opposing nature of the thermal and flow directions slows convection and allows greater diffusion of solute into the fluid domain, thereby thickening the concentration boundary layer. Nevertheless, the general trend remains the same: a higher Dufour number increases concentration, and a higher Soret number decreases it. This behavior matches what was seen in Figure 6 for Maxwell fluids because the thermal and solutal cross-diffusion mechanisms are fundamentally the same.

In Figure 8a, the skin friction coefficient is plotted for the suction case ($S = 0.5$) in a micropolar ternary nanofluid. Here, the Deborah number λ_1, representing the fluid's relaxation time, quantifies how long the fluid retains its memory of deformation. In micropolar fluids, this relates to the delayed response of micro-rotations and velocity gradients. As λ_1 increases, the elasticity becomes more prominent, causing greater resistance to shear deformation, and hence an increase in skin friction. Likewise, an increase in the porosity parameter γ results in greater obstruction to flow within the porous medium, thereby enhancing the skin friction. However, as the mass transfer parameter Nr increases, the negative skin

friction decreases, indicating that stronger outward flow (mass transfer from surface to fluid) diminishes wall shear stress. The concept of negative skin friction arises when the wall shear stress direction is reversed due to dominant mass or momentum transfer away from the surface, a hallmark of a reversed or retarded boundary-layer flow.

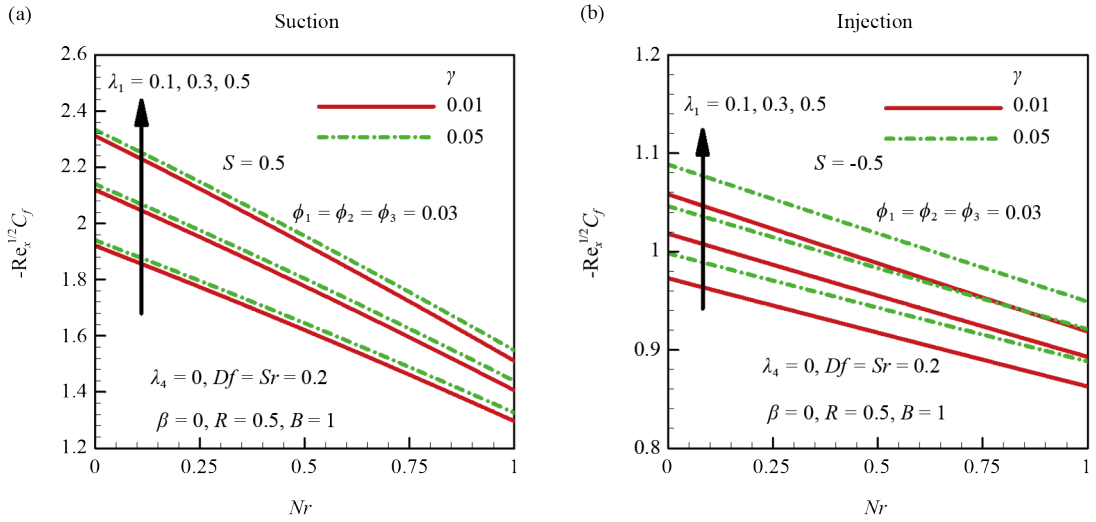


Figure 8. Variation of skin friction with mass transfer in micropolar ternary nanofluids, highlighting the effects of porosity and Deborah number with respect to relaxation time

In Figure 8b, the same variables are examined under the injection condition ($S = -0.5$). Injection pushes fluid from the surface into the boundary layer, reducing shear stress at the wall and resulting in lower overall skin friction than suction. The trends remain similar—higher λ_1 and higher γ both increase the magnitude of negative skin friction by enhancing fluid elasticity and internal resistance, respectively. However, the influence of increasing mass transfer Nr leads to a further reduction in skin friction, as momentum injected into the boundary layer through injection diminishes velocity gradients near the wall. Overall, suction leads to more pronounced wall shear due to the fluid being pulled inward, compressing the boundary layer and increasing velocity gradients near the wall.

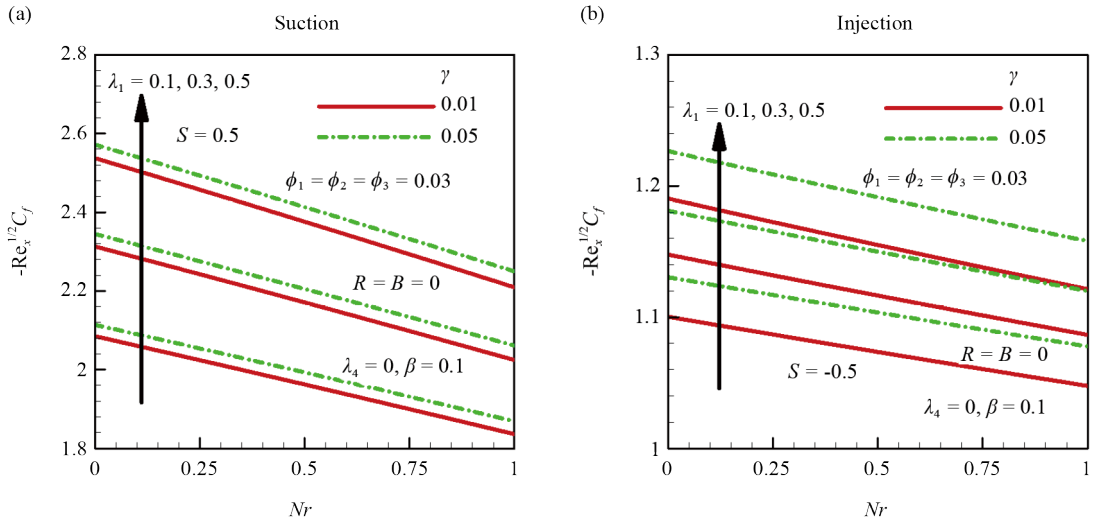


Figure 9. Variation of skin friction with mass transfer in Maxwell ternary nanofluids, highlighting the effects of porosity and Deborah number with respect to relaxation time

In Figure 9a, the suction case ($S = 0.5$) for Maxwell ternary nanofluids is depicted, where the dimensionless skin friction coefficient decreases with increasing mass transfer parameter Nr. In contrast, it increases with γ and the Deborah number λ_1 associated with the relaxation time. The Deborah number in Maxwell fluids quantifies the relative significance of fluid elasticity arising from delayed strain response. Higher λ_1 indicates stronger elastic memory, which resists deformation and leads to greater wall shear, thereby increasing skin friction. Similarly, a higher porosity parameter introduces flow resistance, increasing friction at the boundary. Suction increases skin friction by increasing the inward fluid flux, compressing the boundary layer, and strengthening shear gradients near the wall.

In Figure 9b, the injection scenario ($S = -0.5$) shows similar trends: skin friction diminishes with increasing Nr, but rises with increasing λ_1 and γ. Injection pushes fluid away from the surface, stretching the boundary layer and weakening the near-wall velocity gradient, which reduces skin friction. Despite similar behaviors, Maxwell fluids lack the micro-rotation characteristics of micropolar fluids, so spin viscosity and couple-stress effects are absent in the Maxwell model. Consequently, skin friction values in Maxwell fluids tend to be higher overall compared to micropolar fluids, where microrotation can partially relieve shear stress. This difference explains the slightly elevated friction seen for similar parameter sets. Suction enhances skin friction more significantly than injection because it intensifies momentum diffusion toward the wall.

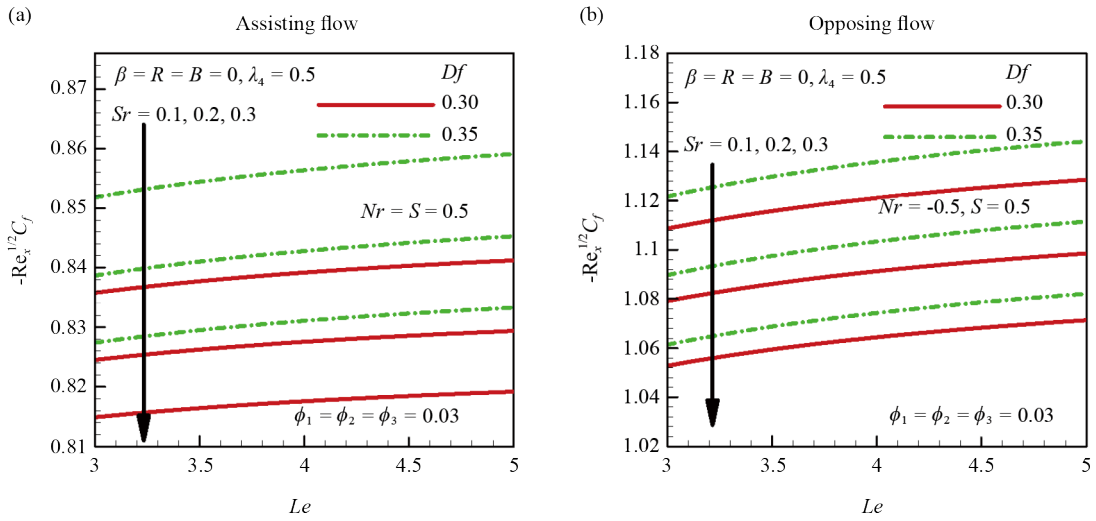


Figure 10. Variation of skin friction with Lewis number in Jeffrey ternary nanofluids, illustrating the effects of Dufour and Soret numbers

In Figure 10a, the skin friction coefficient is shown for assisting flow in a Jeffrey ternary nanofluid ($Nr = S = 0.5$). As Le increases, mass diffusion weakens relative to heat diffusion, thereby enhancing velocity gradients near the wall and increasing the magnitude of negative skin friction. The Soret number (Sr), representing thermophoretic mass flux due to temperature gradients, reduces near-wall shear by promoting mass migration away from the surface, hence decreasing skin friction. The Dufour number (Df) introduces additional heat flux due to concentration gradients. Higher Df strengthens convective heat transfer, thickens the boundary layer, reduces wall shear, and thus lowers skin friction. In assisting flows, buoyancy and the main flow cooperate, reducing resistance and leading to lower overall wall friction.

In Figure 10b, opposing flow conditions are considered ($Nr = -0.5$, $S = 0.5$), where thermal and momentum forces act in opposite directions. This increases flow resistance and compresses the boundary layer, leading to higher skin friction compared to assisting flow. As observed, increasing Le again enhances skin friction due to suppression of mass diffusion. Larger Sr weakens near-wall gradients by moving mass outward, while smaller Df reduces energy added to the system via mass gradients-both effects contribute to lower skin friction. The interaction of opposing forces in this regime intensifies the internal stress distribution in the boundary layer, leading to higher surface friction.

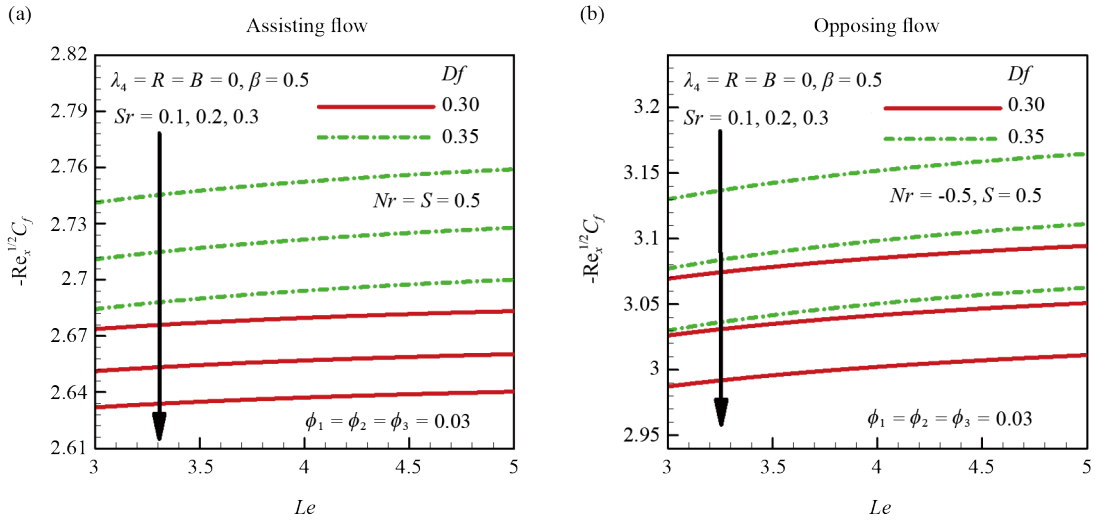


Figure 11. Variation of skin friction with Lewis number in Maxwell ternary nanofluids, illustrating the effects of Dufour and Soret numbers

In Figure 11a, the assisting flow case for Maxwell ternary nanofluids shows the variation in the skin friction coefficient with the Lewis number (Le) for varying Soret (Sr) and Dufour (Df) numbers. The assisting flow ($Nr = S = 0.5$) aligns thermal buoyancy with the free stream, thereby reducing fluid resistance and wall shear. As Le increases, the dominance of thermal diffusion over mass diffusion leads to enhanced temperature-driven momentum transport, which increases skin friction slightly. A rise in Sr reduces wall shear by pushing species outward, while a decrease in Df limits heat feedback from concentration gradients—both acting to diminish skin friction. The overall trend remains consistent with Jeffrey nanofluids, driven by similar cross-diffusion effects, but the magnitude of the skin friction is higher due to stronger viscoelastic resistance in Maxwell models.

In Figure 11b, the opposing flow case ($Nr = -0.5$, $S = 0.5$) is displayed, where thermal and momentum effects act in opposite directions. This causes boundary-layer compression and increases wall shear, resulting in higher skin friction than in the assisting flow. The behavior of skin friction remains the same across varying Le, Sr, and Df: it increases with Le, and decreases with Sr and lower Df. However, due to the opposing nature of the forces, the boundary layer becomes more compact, concentrating velocity gradients near the wall, resulting in a higher friction profile.

In Figure 12a, the suction case ($S = 0.5$) for micropolar ternary nanofluids shows the variation of the local Nusselt number with respect to the mass transfer parameter Nr, Deborah number λ_1, and porosity γ. An increase in Nr indicates a stronger inward flow (mass transfer toward the wall), which enhances thermal gradients near the surface, leading to an increase in the Nusselt number and, consequently, improved convective heat transfer. However, increasing λ_1-characterizing the relaxation time in viscoelastic micropolar fluids—increases elastic resistance, suppressing temperature gradients and reducing the heat transfer rate, thereby decreasing the Nusselt number. Similarly, higher porosity increases internal resistance due to solid-matrix obstruction, reducing fluid mobility and limiting thermal conduction and convection, thereby lowering the Nusselt number. Suction compresses the thermal boundary layer, enhancing the near-wall temperature gradient and thereby increasing heat transfer compared to injection.

In Figure 12b, the injection case ($S = -0.5$) shows similar trends. As Nr increases, outward mass flow strengthens, intensifying surface cooling and thus increasing the Nusselt number. However, higher λ_1 again reduces the rate of heat transport due to the elastic behavior of micropolar fluids, which resist rapid deformation and smear out thermal gradients. Increased porosity also causes dispersion of momentum and energy, reducing effective heat transfer. Compared to suction, injection promotes a thicker thermal boundary layer, thereby weakening the wall temperature gradient and lowering the Nusselt number. Therefore, heat transfer is more efficient under suction due to sharper thermal gradients and more vigorous inward convection.

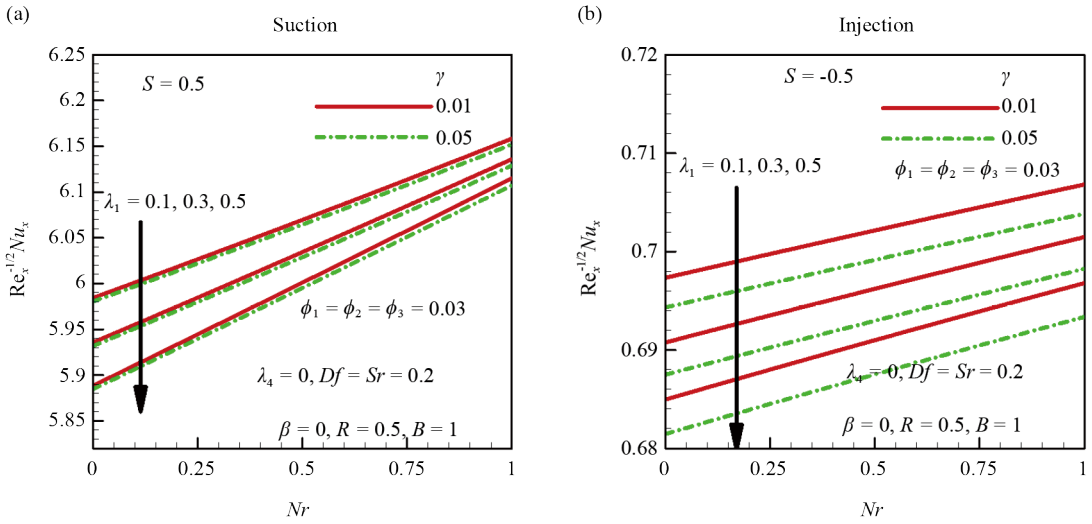


Figure 12. Variation of Nusselt number with mass transfer in micropolar ternary nanofluids, highlighting the effects of porosity and Deborah number with respect to relaxation time

In Figure 13a, the suction case ($S = 0.5$) for Maxwell ternary nanofluids illustrates how the Nusselt number varies with mass transfer Nr, Deborah number λ_1 (linked to relaxation time), and porosity γ. As Nr increases, the inward movement of fluid enhances wall thermal convection, leading to a increase in the Nusselt number. Conversely, increasing λ_1, which characterizes the delayed fluid response in Maxwell-type heat conduction, suppresses thermal gradients, thereby reducing the heat transfer rate. Similarly, higher porosity increases resistance to flow and thermal energy transfer within the porous matrix, leading to a decrease in the Nusselt number. The behavior mirrors that seen in micropolar nanofluids due to the general effect of elastic resistance and structural hindrance on boundary-layer heat transfer.

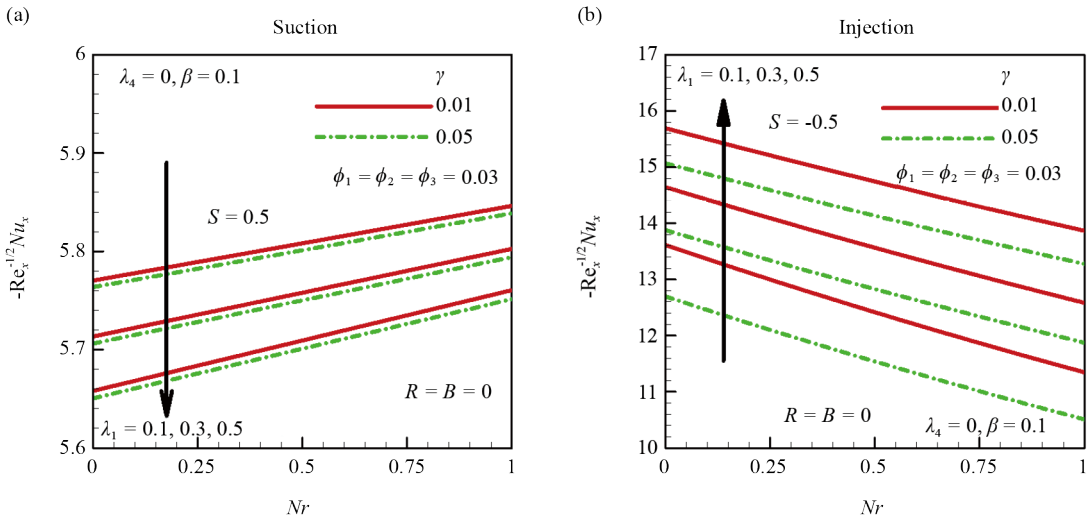


Figure 13. Variation of Nusselt number with mass transfer in Maxwell ternary nanofluids, highlighting the effects of porosity and Deborah number with respect to relaxation time

In Figure 13b, the injection case ($S = -0.5$) exhibits a reversal in behavior: the Nusselt number decreases with increasing Nr. Injection drives fluid away from the wall, weakening the surface temperature gradient and reducing heat transfer efficiency. However, the overall Nusselt number is significantly higher than in the suction case. This is attributed

to the Maxwell fluid's stronger elastic energy storage, which supports sustained thermal transport even when convection is outward. The result is a broader, more thermally active boundary layer under injection, thereby increasing the apparent heat transfer rate. Hence, for Maxwell nanofluids, the Nusselt number under injection exceeds that under suction, unlike in micropolar fluids, where micro-rotational effects can redistribute energy differently.

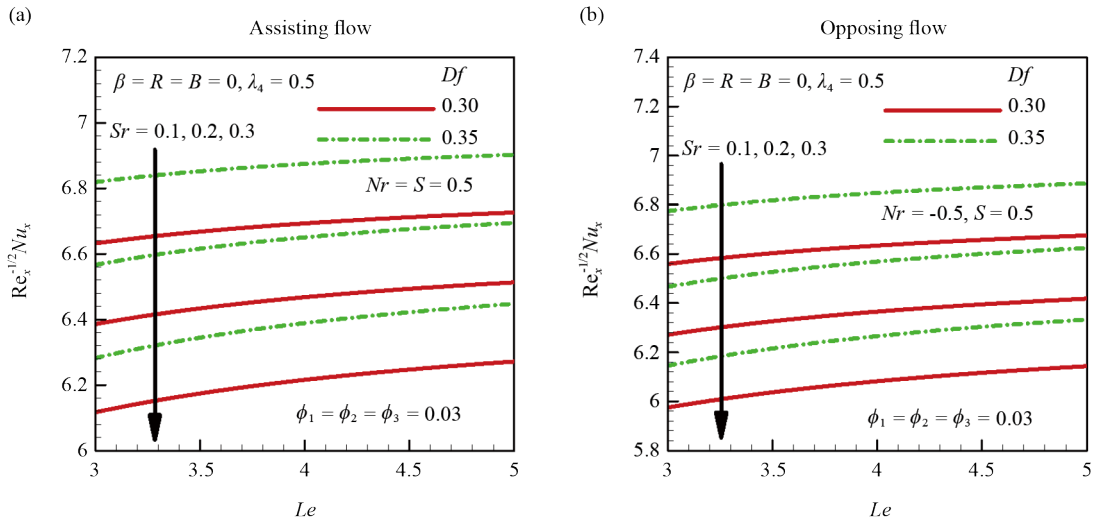


Figure 14. Variation of Nusselt number with Lewis number in Jeffrey ternary nanofluids, illustrating the effects of Dufour and Soret numbers

In Figure 14a, the assisting flow case ($Nr = S = 0.5$) demonstrates the impact of the Lewis (Le), Dufour (Df), and Soret (Sr) numbers on the Nusselt number. As Le increases, thermal diffusion dominates, enhancing heat transfer and raising the Nusselt number. The Dufour number, which represents heat flux due to solute concentration gradients, also supports energy transport; higher Df values intensify this coupling, thereby increasing the Nusselt number. However, higher Soret numbers encourage mass diffusion due to temperature gradients, thereby weakening surface gradients and reducing the Nusselt number. The combined effects support greater heat exchange, assisting flows in which buoyancy and the free stream reinforce thermal transport.

In Figure 14b, the opposing flow case ($Nr = -0.5$, $S = 0.5$) is shown. Here, thermal and hydrodynamic forces counteract each other, disrupting flow stability and reducing energy exchange near the wall. As a result, the Nusselt number is lower compared to the assisting flow case. Despite this, the same parametric trends hold: Nusselt number increases with increasing Le and Df due to more efficient thermal diffusion and solute-coupled heat flux. At the same time, it decreases with increasing Sr, as the outward mass flux dilutes the thermal boundary layer.

In Figure 15a, the assisting flow case ($Nr = S = 0.5$) for Maxwell ternary nanofluids reveals the behavior of the Nusselt number as influenced by the Lewis (Le), Dufour (Df), and Soret (Sr) numbers. As Le increases, thermal diffusivity dominates over mass diffusivity, intensifying temperature gradients near the wall and thereby enhancing heat transfer. Thus, the Nusselt number increases with Le. The Dufour effect, which represents heat flux due to concentration gradients, also reinforces convective heat transfer; thus, higher Df values result in higher Nusselt numbers. Conversely, an increase in Sr enhances solutal diffusion due to temperature gradients, thereby disrupting local thermal gradients near the wall and reducing the Nusselt number. These trends in Maxwell fluids are consistent with their inherent elasticity, which stabilizes heat-conduction mechanisms.

In Figure 15b, the opposing flow case ($Nr = -0.5$, $S = 0.5$) displays similar parametric effects, but with higher Nusselt numbers than in the assisting flow configuration. The opposing nature of buoyancy and free stream induces stronger compression of the thermal boundary layer, thereby increasing thermal gradients and enhancing wall heat transfer. As in the assisting case, increasing Le and Df further boosts heat transfer, whereas increasing Sr opposes it by promoting outward solute migration, thereby weakening thermal retention.

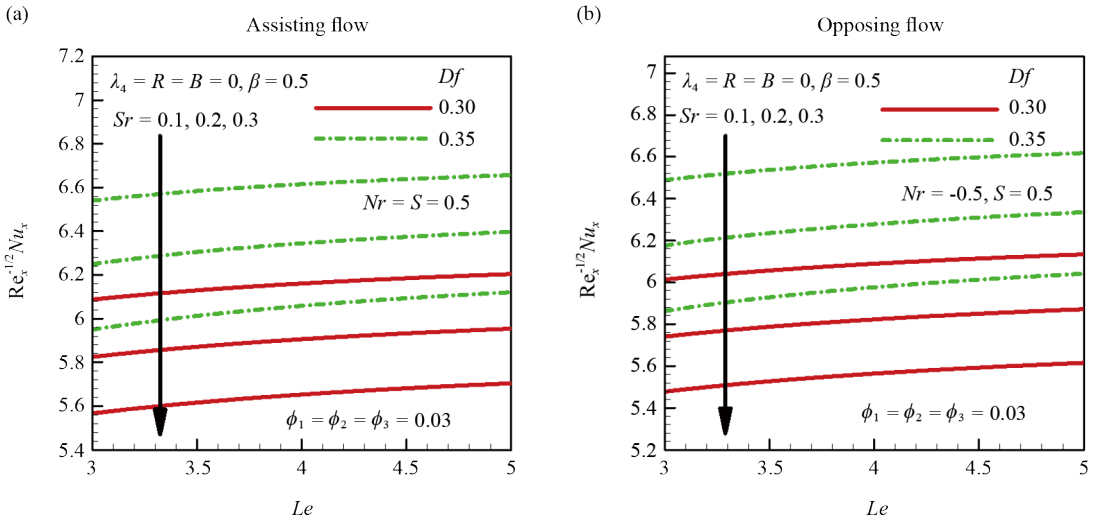


Figure 15. Variation of Nusselt number with Lewis number in Maxwell ternary nanofluids, illustrating the effects of Dufour and Soret numbers

In Figure 16a, the suction case ($S = 0.5$) for micropolar ternary nanofluids illustrates the impact of mass transfer parameter Nr, Deborah number λ_1 related to relaxation time, and porosity γ on the Sherwood number. The Deborah number in micropolar fluids reflects the fluid's elastic response; higher λ_1 increases the relaxation time, delaying the microstructural adjustment to flow and thus dampening solutal transport. This reduces the magnitude of the negative Sherwood number, indicating less mass is being absorbed at the wall. Increased porosity introduces internal resistance to mass transfer, further reducing concentration gradients and lowering the Sherwood number. Suction compresses the concentration boundary layer, enhancing the concentration gradient at the wall and increasing the mass flux, thereby making the Sherwood number more negative and indicating more efficient inward mass transfer.

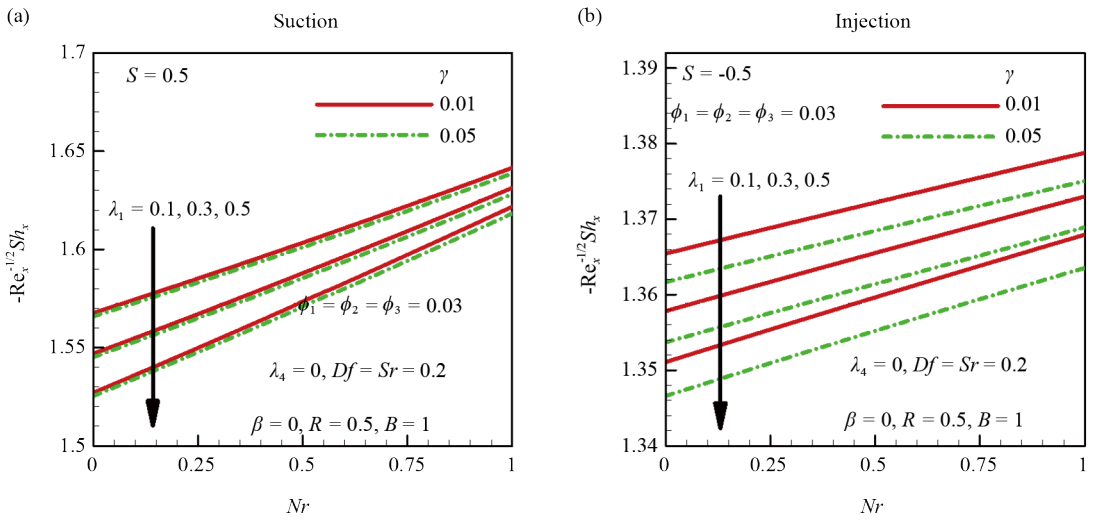


Figure 16. Variation of Sherwood number with mass transfer in micropolar ternary nanofluids, highlighting the effects of porosity and Deborah number with respect to relaxation time

In Figure 16b, under injection conditions ($S = -0.5$), the fluid is pushed away from the wall, thickening the solutal boundary layer and weakening the concentration gradient. This results in a smaller (less negative) Sherwood number

compared to suction. Similar to the suction case, increasing λ_1 increases fluid elasticity and delays solutal diffusion, thereby reducing mass transfer efficiency and decreasing the Sherwood number. Higher porosity again restricts solute mobility through the porous medium, further lowering solutal transport. The Sherwood number becomes more negative with increasing Nr, as more mass is pulled toward or pushed from the surface, depending on the direction of mass transfer. Overall, suction enhances inward mass diffusion and yields stronger negative Sherwood numbers than injection, where wall-normal momentum weakens solute accumulation at the boundary.

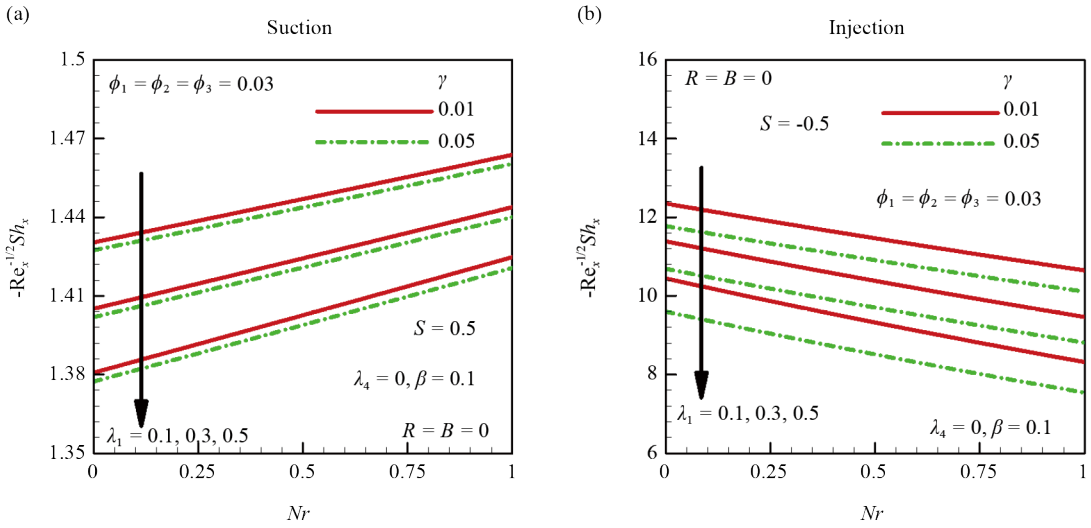


Figure 17. Variation of Sherwood number with mass transfer in Maxwell ternary nanofluids, highlighting the effects of porosity and Deborah number with respect to relaxation time

In Figure 17a, the suction case ($S = 0.5$) for Maxwell ternary nanofluids shows the variation of the dimensionless Sherwood number with mass transfer parameter Nr, Deborah number λ_1, and porosity γ. As suction pulls fluid toward the wall, it enhances inward solute transport and steepens the concentration gradient near the surface, resulting in a more negative Sherwood number, indicative of stronger mass absorption. However, increasing λ_1 introduces a greater relaxation time in Maxwell fluids, reducing the fluid's responsiveness to concentration gradients and thereby dampening mass transfer, thereby reducing the magnitude of the Sherwood number. Similarly, higher porosity impedes mass flow by increasing resistance through the porous medium, further reducing mass absorption at the wall.

In Figure 17b, the injection case ($S = -0.5$) presents a contrasting scenario. Injection expels fluid from the wall, generally weakening the concentration gradient and thus reducing mass transfer. However, in the presence of Maxwell nanofluids, the fluid's elastic character helps sustain concentration gradients even under outward flow, leading to a higher Sherwood number than in the suction case. The same trend is observed: higher λ_1 and γ reduce the effectiveness of mass transfer by introducing relaxation and structural drag, respectively. Yet, due to the elasticity of Maxwell fluids and the altered boundary-layer dynamics under injection, mass transport becomes more pronounced, especially in the presence of strong solutal diffusion, explaining the elevated Sherwood values under injection. This behavior reflects the unique viscoelastic advantage of Maxwell fluids in sustaining diffusion-dominated transport under reversed flow conditions.

In Figure 18a, the assisting flow case ($Nr = S = 0.5$) for Jeffrey ternary nanofluids presents the variation of the Sherwood number with Lewis (Le), Dufour (Df), and Soret (Sr) numbers. As Le increases, thermal diffusion dominates solutal diffusion, sharpening the concentration gradient near the wall and increasing the magnitude of the negative Sherwood number, indicating enhanced mass absorption. A decrease in Df reduces the energy contribution from solute gradients, weakening solutal transport and reducing mass transfer. Higher Soret numbers promote outward mass diffusion driven by temperature gradients, thereby counteracting solute accumulation at the wall and decreasing the Sherwood

number. In assisting flows, momentum and buoyancy forces reinforce each other, promoting smoother, less resisted solute transport but yielding lower overall Sherwood numbers than in opposing cases.

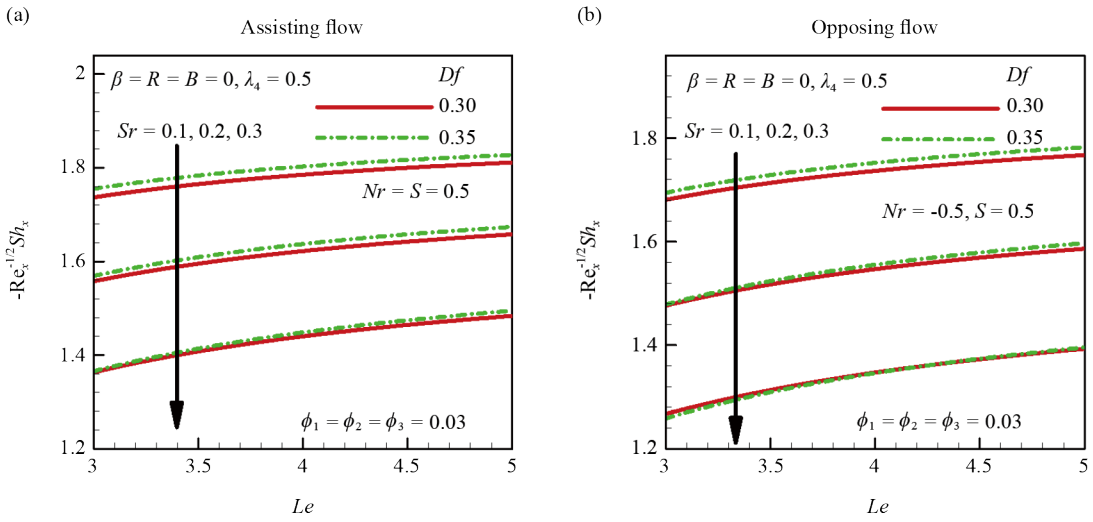


Figure 18. Variation of Sherwood number with Lewis number in Jeffrey ternary nanofluids, illustrating the effects of Dufour and Soret numbers

In Figure 18b, the opposing flow case ($Nr = -0.5$, $S = 0.5$) demonstrates stronger solute gradient development due to compression of the solutal boundary layer, which leads to a higher Sherwood number than in the assisting flow case. Though the trends with Le, Df, and Sr remain the same—increasing Le enhances, increasing Sr reduces, and decreasing Df weakens mass transfer—the opposing nature of the flow forces enhances boundary-layer compactness and increases the wall-normal solute gradient. This increases inward diffusion, thereby intensifying the mass transfer rate. In Jeffrey fluids, the presence of both relaxation and retardation time components enables a smoother response to dynamic opposing flow conditions, efficiently sustaining sharp gradients and leading to higher Sherwood numbers.

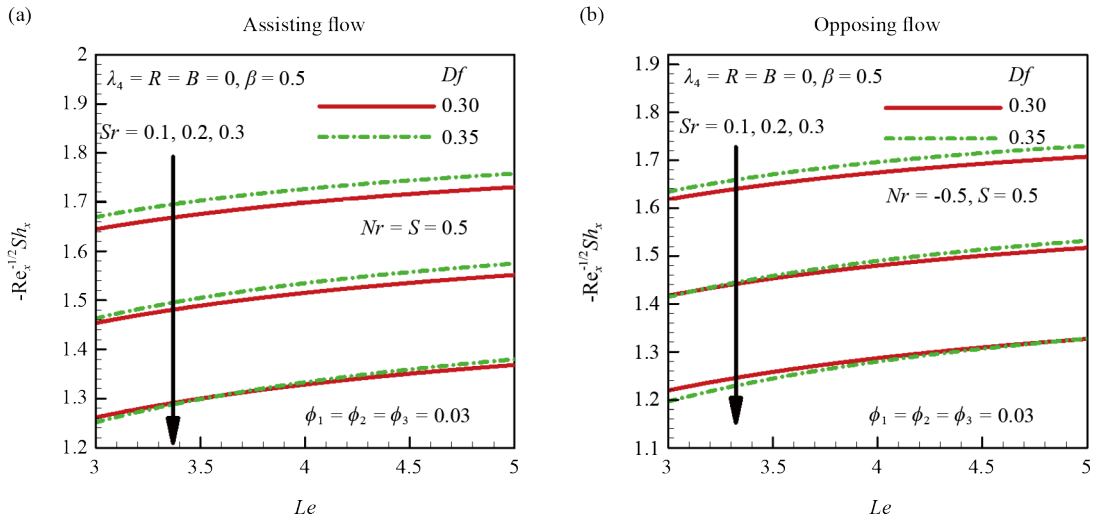


Figure 19. Variation of Sherwood number with Lewis number in Maxwell ternary nanofluids, illustrating the effects of Dufour and Soret numbers

In Figure 19a, for the assisting flow of Maxwell ternary nanofluids, the Sherwood number is negative and increases in magnitude with increasing Lewis number Le. This indicates that the solutal boundary layer thickens and that mass transfer decreases downstream. The negative Sherwood number implies a net mass flux from the fluid to the wall, characteristic of reverse species diffusion, or back diffusion, in ternary systems, especially under strong thermophoretic and Brownian motion influences. The polymeric nature of the Maxwell fluid resists rapid deformation and mass transport, leading to a moderate increase in the Sherwood number with higher Le, particularly evident when comparing the diffusivity factors $Df = 0.30$ and $Df = 0.35$.

In Figure 19b, the trend for opposing flow shows similar negative Sherwood behavior, but with slightly lower values than in assisting flow, due to adverse pressure gradients opposing the flow direction. This increases the tendency toward flow separation and decreases convective mass transfer efficiency. Here too, the non-Newtonian Maxwell fluid properties suppress rapid mass diffusion, and the negative Sherwood number remains evident across varying Sr. The influence of negative Nr suggests that thermophoresis is countering the Soret effect, further amplifying the negative concentration gradients near the wall.

5. Comparison between Jeffrey, Maxwell, and Micropolar ternary nanofluids

The heat transfer behavior of Jeffrey and Maxwell ternary nanofluids stems from their inherent viscoelastic nature but diverges due to their rheological formulations. Maxwell fluids have a single relaxation time, emphasizing elastic recovery and enabling them to retain thermal energy under high-strain conditions, especially in opposing flows. This strong elastic memory enhances boundary layer confinement and results in relatively higher Nusselt numbers. Jeffrey fluids, however, incorporate both relaxation and retardation times. This dual mechanism introduces a more adaptive response to deformation, leading to smoother temperature gradients and slightly lower heat transfer rates than in Maxwell fluids. When extended to include micropolar ternary nanofluids, the distinctions become more nuanced. Micropolar fluids allow the inclusion of microrotation and spin viscosity, which provide additional mechanisms for energy and momentum diffusion. This can cause a redistribution of thermal gradients within the boundary layer, occasionally reducing overall thermal efficiency. Unlike the purely viscoelastic Maxwell and Jeffrey models, micropolar fluids introduce microstructural effects that can soften or reorient the flow and heat-transfer profiles.

From a mass transfer standpoint, Jeffrey fluids exhibit higher negative Sherwood numbers than both Maxwell and micropolar fluids in both assisting and opposing flows. The combination of relaxation and retardation allows Jeffrey fluids to resist shear while accommodating delayed deformation, thereby fostering a broader, more diffuse concentration boundary layer. Maxwell fluids, though elastic, lack the retardation component, resulting in narrower species diffusion profiles and slightly lower negative Sherwood numbers. In contrast, micropolar fluids, due to their inherent couple-stress effects, tend to weaken concentration gradients, resulting in the lowest back-diffusion among the three.

For skin friction and wall shear stress, Maxwell fluids display a stiffer response due to pure relaxation behavior, which increases elastic recoil and results in higher wall shear under similar conditions. Jeffrey fluids, due to their dual-time framework, moderate this response, providing smoother transitions and better control over wall stress distribution. Micropolar fluids again differ by redistributing shear through microrotation, often reducing the effective skin friction by diverting part of the momentum into spin motion.

6. Concluding remarks

The concluding analysis consolidates the key thermal and solutal behaviors observed in each fluid model. Comparative performance across flow conditions highlights the superior heat-transfer efficiency of Maxwell fluids and the solutal-diffusion advantage of Jeffrey fluids. The influence of microstructure in micropolar fluids provides nuanced control over skin friction and concentration profiles. The study underscores the design potential of using aspect ratio, porosity, and flow manipulation to optimize electrothermal systems using complex nanofluid mixtures. The key findings are summarized below:

• Maxwell fluids exhibit the highest Nusselt numbers, particularly under opposing flows, due to their strong elastic memory.

• Jeffrey fluids demonstrate higher Sherwood numbers, indicating superior mass transfer efficiency in both assisting and opposing flow cases.

• Micropolar fluids reduce skin friction via microrotation, resulting in smoother velocity gradients near walls.

• Suction enhances wall shear stress and the Nusselt number, while injection reduces them, with changes up to 30% in the thermal boundary layer thickness.

• Increasing Deborah numbers (λ_1, λ_4) in all fluids significantly alters velocity and angular profiles—stronger retardation increases flow, while relaxation suppresses it.

• Higher Soret numbers reduce temperature and concentration near the wall, while higher Dufour numbers boost both heat and mass transfer.

• Porosity acts as a resistance parameter, generally reducing skin friction, Nusselt, and Sherwood numbers across all fluids.

• A tri-hybrid nanofluid comprising MWCNT, GO, and MoS_2 provides an optimal balance between thermal conductivity and viscosity control.

7. Future extensions of this study

Future work could extend this framework by incorporating magnetic field effects (MHD), rotation, or time-dependent stretching surfaces to simulate real-world thermal systems better. Additionally, investigating fractional-order models or using machine learning for parametric sensitivity analysis and optimization could yield more profound insights. Experimental validation of tri-hybrid nanofluid formulations using lab-scale setups would also bridge the gap between theoretical predictions and practical implementation. Moreover, exploring behavior in turbulent or transitional flow regimes within complex geometries could further broaden the applicability of these advanced nanofluids.

Acknowledgments

The authors extend their appreciation to Prince Sattam bin Abdulaziz University for funding this research work through the project number (PSAU/2025/01/36908). There was no additional external funding received for this study.

Data availability statement

The data that support the findings of this study are available from the corresponding author upon reasonable request.

Conflict of interest

The authors declare no conflict of interest.

References

[1] Noreen S, Waheed S, Lu D, Hussanan A. Heat measures in performance of electroosmotic flow of Williamson fluid in micro-channel. *Alexandria Engineering Journal*. 2020; 59(6): 4081-4100. Available from: https://doi.org/10.1016/j.aej.2020.07.013.

[2] Aldabesh A, Khan SU, Habib D, Waqas H, Tlili I, Khan MI, et al. Unsteady transient slip flow of Williamson nanofluid containing gyrotactic microorganism and activation energy. *Alexandria Engineering Journal*. 2020; 59(6): 4315-4328. Available from: https://doi.org/10.1016/j.aej.2020.07.036.

[3] Kahshan M, Lu D, Rahimi-Gorji M, Do HT. A mathematical model of blood flow in a permeable channel: application to flat plate dialyzer. *Physica Scripta*. 2020; 95(4): 045202. Available from: https://doi.org/10.1088/1402-4896/ab588e.

[4] Hanif H. A computational approach for boundary layer flow and heat transfer of fractional Maxwell fluid. *Mathematics and Computers in Simulation*. 2022; 191: 1-13. Available from: https://doi.org/10.1016/j.matcom.2021.07.024.

[5] Amer QM. Numerical simulation of heat transfer flow subject to MHD of Williamson nanofluid with thermal radiation. *Symmetry*. 2021; 13(1): 10. Available from: https://doi.org/10.3390/sym13010010.

[6] Thenmozhi D, Rao ME, Devi RR. Analysis of Jeffrey on MHD flow with stretching porous sheets of heat transfer system. *Forces in Mechanics*. 2023; 11: 100180. Available from: https://doi.org/10.1016/j.finmec.2023.100180.

[7] Raje A, Bhise AA, Kulkarni A. Entropy analysis of the MHD Jeffrey fluid flow in an inclined porous pipe with convective boundaries. *International Journal of Thermofluids*. 2023; 17: 100275. Available from: https://doi.org/10.1016/j.ijft.2022.100275.

[8] Li D, Dong J, Li H. Analysis of pulse electromagnetic electroosmotic flow of Jeffrey fluid through parallel plate microchannels under a constant pressure gradient. *Journal of Molecular Liquids*. 2023; 390: 123034. Available from: https://doi.org/10.1016/j.molliq.2023.123034.

[9] Choi SUS. Enhancing thermal conductivity of fluids with nanoparticles. In: *The Proceedings of the 1995 ASME International Mechanical Engineering Congress and Exposition*. San Francisco, CA, USA: ASME; 1995. p.99-105.

[10] Chen CH. Effect of viscous dissipation on heat transfer in a non-Newtonian liquid film over an unsteady stretching sheet. *Journal of Non-Newtonian Fluid Mechanics*. 2005; 135(2-3): 128-135. Available from: https://doi.org/10.1016/j.jnnfm.2006.01.009.

[11] Hayat T, Imtiaz M, Alsaedi A, Mansoor R. MHD flow of nanofluids over an exponentially stretching sheet in a porous medium with convective boundary conditions. *Chinese Physics B*. 2014; 23(5): 054701. Available from: https://doi.org/10.1088/1674-1056/23/5/054701.

[12] Alla AMA, Dahab SMA. Magnetic field and rotation effects on peristaltic transport of Jeffrey fluid in an asymmetric channel. *Journal of Magnetism and Magnetic Materials*. 2015; 374: 680-689. Available from: https://doi.org/10.1016/j.jmmm.2014.08.091.

[13] Hayat T, Hussain T, Shehzad SA, Alsaedi A. Flow of Oldroyd-B fluid with nanoparticles and thermal radiation. *Applied Mathematics and Mechanics (English Edition)*. 2015; 36(1): 69-80. Available from: https://doi.org/10.1007/s10483-015-1896-9.

[14] Irfan M, Muhammad T. Numerical simulation of bioconvection radiative heat transport flow of MHD Carreau nanofluid. *ZAMM-Journal of Applied Mathematics and Mechanics*. 2024; 104(11): e202300813. Available from: https://doi.org/10.1002/zamm.202300813.

[15] Rashid M, Irfan M, Muhammad T, Abu-Jrai A, Anwar MS. Dynamics of solar radiation absorption for Darcy-Forchheimer Carreau nanofluid considering variable conductivity with chemical reaction: a solar thermal energy application. *Results in Engineering*. 2025; 26: 104670. Available from: https://doi.org/10.1016/j.rineng.2025.104670.

[16] Hamida MBB, Irfan M, Puthalath AK, Shoaib M. Bioconvection behavior in radiative MHD Maxwell nanofluids with gyrotactic motile microorganisms: toward enhanced solar thermal energy performance. *Journal of Thermal Analysis and Calorimetry*. 2025; 150: 15969-15983. Available from: https://doi.org/10.1007/s10973-025-14830-4.

[17] Hamida MBB, Irfan M, Anwar MS, Javed M. Solar radiation-driven MHD Maxwell nanofluid flow with gyrotactic microorganisms and Soret-Dufour effects: a thermal engineering study. *Journal of Radiation Research and Applied Sciences*. 2025; 18(4): 101887. Available from: https://doi.org/10.1016/j.jrras.2025.101887.

[18] Hussain S, Oztop HF, Jamal M, Hamdeh NA. Double diffusive nanofluid flow in a duct with cavity heated from below. *International Journal of Mechanical Sciences*. 2017; 131-132: 535-545. Available from: https://doi.org/10.1016/j.ijmecsci.2017.07.057.

[19] Khan M, Irfan M, Khan WA, Alshomrani AS. A new modeling for 3D Carreau fluid flow considering nonlinear thermal radiation. *Results in Physics*. 2017; 7: 2692-2704. Available from: https://doi.org/10.1016/j.rinp.2017.07.024.

[20] Arif M, Ali F, Sheikh NA, Khan I. Enhanced heat transfer in working fluids using nanoparticles with ramped wall temperature: applications in engine oil. *Advances in Mechanical Engineering*. 2019; 11(11): 1687814019880987. Available from: https://doi.org/10.1177/1687814019880987.

[21] Zeb S, Gul S, Shah K, Santina D, Mlaiki NM. Melting heat transfer and thermal radiation effects on MHD tangent hyperbolic nanofluid flow with chemical reaction and activation energy. *Thermal Science*. 2023; 27(1): 253-261.

[22] Sulgani MT, Karimipour A. Improve the thermal conductivity of 10w40-engine oil at various temperatures by the addition of Al_2O_3/Fe_2O_3 nanoparticles. *Journal of Molecular Liquids*. 2019; 283: 660-666. Available from: https://doi.org/10.1016/j.molliq.2019.03.140.

[23] Said Z, Sundar LS, Tiwari AK, Ali HM, Sheikholeslami M, Bellos E, et al. Recent advances on the fundamental physical phenomena behind stability, dynamic motion, thermophysical properties, heat transport, applications, and challenges of nanofluids. *Physics Reports*. 2022; 946: 1-94. Available from: https://doi.org/10.1016/j.physrep.2021.07.002.

[24] Qiu L, Zhu N, Feng Y, Michaelides EE, Żyła G, Jing D, et al. A review of recent advances in thermophysical properties at the nanoscale: from solid state to colloids. *Physics Reports*. 2020; 843: 1-81. Available from: https://doi.org/10.1016/j.physrep.2019.12.001.

[25] Smith SR, Rafati R, Haddad AS, Cooper A, Hamidi H. Application of aluminium oxide nanoparticles to enhance rheological and filtration properties of water based muds at HPHT conditions. *Colloids and Surfaces A: Physicochemical and Engineering Aspects*. 2018; 537: 361-371. Available from: https://doi.org/10.1016/j.colsurfa.2017.10.050.

[26] Asjad MI, Ikram MD, Ali R, Baleanu D, Alshomrani AS. New analytical solutions of heat transfer flow of clay-water base nanoparticles with the application of novel hybrid fractional derivative. *Thermal Science*. 2020; 24(1): 343-350.

[27] Aramendiz J, Imqam A. Water-based drilling fluid formulation using silica and graphene nanoparticles for unconventional shale applications. *Journal of Petroleum Science and Engineering*. 2019; 179: 742-749. Available from: https://doi.org/10.1016/j.petrol.2019.04.085.

[28] Tian XX, Kalbasi R, Qi C, Karimipour A, Huang HL. Efficacy of hybrid nano-powder presence on the thermal conductivity of the engine oil: an experimental study. *Powder Technology*. 2020; 369: 261-269. Available from: https://doi.org/10.1016/j.powtec.2020.05.004.

[29] Bumataria RK, Chavda NK, Panchal H. Current research aspects in mono and hybrid nanofluid-based heat pipe technologies. *Heliyon*. 2019; 5(5): e01627. Available from: https://doi.org/10.1016/j.heliyon.2019.e01627.

[30] Yang L, Ji W, Mao M, Huang JN. An updated review on the properties, fabrication and application of hybrid-nanofluids along with their environmental effects. *Journal of Cleaner Production*. 2020; 257: 120408. Available from: https://doi.org/10.1016/j.jclepro.2020.120408.

[31] Khan MR, Pan K, Khan AU, Nadeem S. Dual solutions for mixed convection flow of SiO_2-Al_2O_3/water hybrid nanofluid near the stagnation point over a curved surface. *Physica A: Statistical Mechanics and Its Applications*. 2020; 547: 123959. Available from: https://doi.org/10.1016/j.physa.2019.123959.

[32] Tlili I, Bhatti MM, Hamad SM, Barzinjy AA, Sheikholeslami M, Shafee A. Macroscopic modeling for convection of hybrid nanofluid with magnetic effects. *Physica A: Statistical Mechanics and Its Applications*. 2019; 534: 122136. Available from: https://doi.org/10.1016/j.physa.2019.122136.

[33] Arif M, Kumam P, Kumam W, Mostafa Z. Heat transfer analysis of radiator using different shaped nanoparticles water-based ternary hybrid nanofluid with applications: a fractional model. *Case Studies in Thermal Engineering*. 2022; 31: 101837. Available from: https://doi.org/10.1016/j.csite.2022.101837.

[34] Zeb H, Shah K, Alqudah M, Abdeljawad T. Variable thermal conductivity effects on MHD flow of non-Newtonian ternary hybrid nanofluid between rotating disks: a Cattaneo-Christov heat transfer analysis. *Case Studies in Thermal Engineering*. 2025; 71: 106119. Available from: https://doi.org/10.1016/j.csite.2025.106119.

[35] Xuan Z, Zhai Y, Ma M, Li Y, Wang H. Thermo-economic performance and sensitivity analysis of ternary hybrid nanofluids. *Journal of Molecular Liquids*. 2021; 323: 114889. Available from: https://doi.org/10.1016/j.molliq.2020.114889.

[36] Ahmed W, Kazi SN, Chowdhury ZZ, Johan MRB, Mehmood S, Soudagar MEM, et al. Heat transfer growth of sono chemically synthesized novel mixed metal oxide ZnO + Al_2O_3 + TiO_2/DW based ternary hybrid nanofluids in a square flow conduit. *Renewable and Sustainable Energy Reviews*. 2021; 145: 111025. Available from: https://doi.org/10.1016/j.rser.2021.111025.

[37] Adun H, Kavaz D, Wole-Osho I, Dagbasi M. Synthesis of Fe_3O_4-Al_2O_3-ZnO/water ternary hybrid nanofluid: investigating the effects of temperature, volume concentration, and mixture ratio on specific heat capacity and development of hybrid machine learning for prediction. *Journal of Energy Storage*. 2021; 41: 102947. Available from: https://doi.org/10.1016/j.est.2021.102947.

[38] Liu F, Zhuang P, Liu Q. *Numerical Methods of Fractional Partial Differential Equations and Applications*. Science Press; 2015.

[39] Liu F, Feng L, Anh V, Li J. Unstructured-mesh Galerkin finite element method for the two-dimensional multi-term time-space fractional Bloch-Torrey equations on irregular convex domains. *Computers and Mathematics with Applications*. 2019; 78(5): 1637-1650. Available from: https://doi.org/10.1016/j.camwa.2019.01.007.

[40] Sun HG, Zhang Y, Baleanu D, Chen W, Chen YQ. A new collection of real world applications of fractional calculus in science and engineering. *Communications in Nonlinear Science and Numerical Simulation*. 2018; 64: 213-231. Available from: https://doi.org/10.1016/j.cnsns.2018.04.019.

[41] Kamran N, Asif M, Shah K, Abdalla B, Abdeljawad T. Numerical solution of Bagley-Torvik equation including Atangana-Baleanu derivative arising in fluid mechanics. *Results in Physics*. 2023; 49: 106468. Available from: https://doi.org/10.1016/j.rinp.2023.106468.

[42] Ahmad SW, Sarwar M, Shah K, Eiman, Abdeljawad T. Study of a coupled system with sub-strip and multi-valued boundary conditions via topological degree theory on an infinite domain. *Symmetry*. 2022; 14(5): 841. Available from: https://doi.org/10.3390/sym14050841.

[43] El-Gazar EF, Hassan H, Rabia SI, Zahra WK. Study of the impact of using hybrid nanofluid and saline water preheating on the performance of both integrated solar still and photovoltaic panel using fractional modeling. *European Physical Journal Plus*. 2021; 136: 717. Available from: https://doi.org/10.1140/epjp/s13360-021-01654-y.

[44] El-Gazar EF, Zahra WK, Hassan H, Rabia SI. Fractional modeling for enhancing the thermal performance of conventional solar still using hybrid nanofluid: energy and exergy analysis. *Desalination*. 2021; 503: 114847. Available from: https://doi.org/10.1016/j.desal.2020.114847.

[45] Nadeem S, Haq RU, Khan ZH. Numerical study of MHD boundary layer flow of a Maxwell fluid past a stretching sheet in the presence of nanoparticles. *Journal of the Taiwan Institute of Chemical Engineers*. 2014; 45(1): 121-126. Available from: https://doi.org/10.1016/j.jtice.2013.04.006.

[46] Ramzan M, Bilal M, Chung JD, Farooq U. Mixed convective flow of Maxwell nanofluid past a porous vertical stretched surface: an optimal solution. *Results in Physics*. 2016; 6: 1072-1079. Available from: https://doi.org/10.1016/j.rinp.2016.11.036.

[47] Kim J, Kang YT, Choi CK. Analysis of convective instability and heat transfer characteristics of nanofluids. *Physics of Fluids*. 2004; 16(7): 2395-2401. Available from: https://doi.org/10.1063/1.1739247.

[48] Wang X, Mujumdar AS. Heat transfer characteristics of nanofluids: a review. *International Journal of Thermal Sciences*. 2007; 46(1): 1-19. Available from: https://doi.org/10.1016/j.ijthermalsci.2006.06.010.

[49] Anoop KB, Kabelac S, Sundararajan T, Das SK. Rheological and flow characteristics of nanofluids: influence of electroviscous effects and particle agglomeration. *Journal of Applied Physics*. 2009; 106(3): 034909. Available from: https://doi.org/10.1063/1.3182807.

[50] Ghadikolaei SS, Yassari M, Sadeghi H, Hossienzadeh K, Ganji DD. Investigation on thermophysical properties of TiO_2-Cu/H_2O hybrid nanofluid transport dependent on shape factor in MHD stagnation point flow. *Powder Technology*. 2017; 322: 428-438. Available from: https://doi.org/10.1016/j.powtec.2017.09.006.

[51] Shi L, He Y, Hu Y, Wang X. Thermophysical properties of Fe_3O_4-CNT nanofluid and controllable heat transfer performance under magnetic field. *Energy Conversion and Management*. 2018; 177: 249-257. Available from: https://doi.org/10.1016/j.enconman.2018.09.046.

[52] Nguyen HT, Hakimeh M, Shahram R. A mathematical model for COVID-19 transmission by using the Caputo fractional derivative. *Chaos, Solitons and Fractals*. 2020; 140: 110107. Available from: https://doi.org/10.1016/j.chaos.2020.110107.

[53] Nazar R, Amin N, Pop I. Mixed convection boundary-layer flow from a horizontal circular cylinder in micropolar fluids: case of constant wall temperature. *International Journal of Numerical Methods for Heat and Fluid Flow*. 2003; 13(1): 86-109. Available from: https://doi.org/10.1108/09615530310456778.

[54] Ishak A, Nazar R, Pop I. Heat transfer over an unsteady stretching permeable surface with prescribed wall temperature. *Nonlinear Analysis: Real World Applications*. 2009; 10(5): 2909-2913. Available from: https://doi.org/10.1016/j.nonrwa.2008.09.010.

[55] Hayat T, Qasim M, Mesloub S. MHD flow and heat transfer over permeable stretching sheet with slip conditions. *International Journal for Numerical Methods in Fluids*. 2011; 66(8): 963-975. Available from: https://doi.org/10.1002/fld.2294.

[56] Hayat T, Mustafa M, Pop I. Heat and mass transfer for Soret and Dufour's effect on mixed convection boundary layer flow over a stretching vertical surface in a porous medium filled with a viscoelastic fluid. *Communications in Nonlinear Science and Numerical Simulation*. 2010; 15(5): 1183-1196. Available from: https://doi.org/10.1016/j.cnsns.2009.05.062.